1

Recent weathering promotes C storage inside large phyllosilicate particles in forest soil

4

Ingride Van Der Kellen[1], Delphine Derrien[1], Jaafar Ghanbaja[2], Marie-Pierre Turpault[1,*]

[1] INRAE, BEF, F-54000 Nancy, France

[2] Université de Lorraine, CNRS, IJL, F-54000 Nancy, France

*Corresponding author

Marie-Pierre Turpault

marie-pierre.turpault@inrae.fr

INRAE, BEF, Route d'Amance, 54280 Champenoux, France

Abstract

Mineral weathering in soils is expected to promote chemical and physical interactions between soil organic matter and mineral phases, which are known to enhance the protection of organic matter from decomposition. The investigation of mineral-organic associations (MOAs) formation during weathering is therefore crucial to understanding carbon storage processes in soils. Until now studies have been mainly conducted by building inferences from soil characteristics, through short-term laboratory experiments in simplified conditions, or over very long-term time scales using soil chronosequences. Weathering can significantly alter the mineral matrix at the annual timescale, but knowledge regarding MOA formation processes occurring *in situ*, over short time scales and during the first stage of mineral weathering is lacking.

To fill this gap, we performed a mesh bag incubation containing large Na-saturated and organic carbon-free vermiculite particles (200-400 μm in size) in acidic soil of a Douglas-fir forest, in the Beaujolais area (France). The vermiculite bags were deposited at the interface

between the forest floor and the mineral soil, where intense weathering occurs. After 20 years of soil incubation, the weathered vermiculite particles were collected and characterized at the macroscale (X ray diffraction and physicochemical analyses), at the microscale (scanning electron microscopy-SEM imaging and element mapping) and at the nanoscale (transmission electron microscopy-TEM imaging, element mapping and speciation by electron energy loss spectroscopy-EELS) on a focus ion beam (FIB) section exposing the inside section of vermiculite particles.

Cation exchange capacity, exchangeable cations and elemental analysis of the vermiculite particles showed important changes after 20 years of incubation. The initial exchangeable Na pool was completely depleted. The cation exchange capacity strongly decreased from 178.1 $cmol_c$ kg^{-1} to 49.2 $cmol_c$ kg^{-1} due to interlayer hydroxylation of the weathered vermiculite. The weathering budget indicated a 10% vermiculite dissolution and an organic carbon (C) enrichment of 5 mg g^{-1}.

Microscope images and elemental mapping of control vermiculite particles (nonincubated) showed a flat, smooth surface morphology with no detected C. In contrast, 20-year weathered vermiculite particles showed irregular outer- and inner-surfaces marked by multiple cracks from chemical dissolution. Some nano- and microscale exfoliation spaces filled with C were observed inside the weathered particles. C in association with Ca occurred in nanoscale exfoliation spaces. C also occurred entrapped in nanocrystalline Mn oxides (hausmannite) or K-rich aluminosilicates, which precipitated in micro-sized exfoliation spaces. These observations indicated that C storage inside the altered vermiculite particles was both mediated by chemical binding and physical entrapment. The functional groups of the organic matter revealed by EELS spectroscopy strongly differed between nano- and microscale exfoliation spaces.

This study using the mineral bag incubation method provides evidence of new processes driving C storage inside large phyllosilicate particles during their initial and recent weathering, which could contribute to long-term C stabilization.

Abbreviations

V0 – control vermiculite at the macro- and microscale;

V20 – weathered vermiculite at the macro- and microscale;

V0n – control vermiculite matrix at the nanoscale;

V20n – weathered vermiculite matrix at the nanoscale;

MnOx – manganese oxide deposit;

SiAl – aluminosilicate;

SiAlK – K-rich aluminosilicate

Keywords

Phyllosilicate recent weathering, organic carbon, exfoliation spaces, mineral-organic association, coprecipitation, Mn oxide

1 Introduction

Soil is the most important terrestrial carbon (C) sink at the global scale containing three times more carbon than the atmosphere (2400 GtC vs. 800 GtC) (Camino-Serrano et al., 2018). Soils can behave as sinks or sources, depending on their biogeophysicochemical properties, climate, land-use and agricultural or silvicultural practices (Dignac et al., 2017). Soil minerals play a key-role in soil organic matter (SOM) storage and stabilization (Schmidt et al., 2011; Mathieu et al., 2015; Hemingway et al., 2019; Mikutta et al., 2019). Indeed up to 90% of the total organic phases can be associated with minerals (Mikutta et al., 2019). Plant-, fauna- and microbe-derived organic compounds can all be engaged in mineral organic associations (MOAs). Molecules derived from microbial products are considered as the main promoters of stable MOAs (Miltner et al., 2012; Clemmensen et al., 2013; Cotrufo et al., 2015; Lavallee et al., 2018) because of their higher oxidation degree and polarity, which are responsible for a higher reactivity toward mineral particles compared with plant organic

78   moieties (Lehmann and Kleber, 2015; Wang et al., 2017). Mineral phases are responsible for

79   both physical and chemical protection of SOM (Kleber et al., 2021). They physically isolate

80   SOM from decomposers by entrapment in their microporosities (Kleber et al., 2015; Johnson

81   et al., 2015) and provide chemically reactive surfaces for organic moieties adsorption

82   (Remusat et al., 2012; Vogel et al., 2014; Basile-Doelsch et al., 2020). Mechanisms of SOM

83   protection by minerals are generated by multiple biotic and abiotic processes (Schmidt et al.,

84   2011; Dignac et al., 2017) and include mineral weathering that enhances mineral reactivity

85   toward organic moieties (Basile-Doelsch et al., 2015). Recent weathering can significantly

86   alter minerals and the annual timescale, even in temperate regions (Turpault et al., 2007;

87   Barré et al., 2008). At the geological timescale C removal from the atmosphere during silicate

88   weathering, followed by C deposition as carbonate in the oceans, is well documented

89   (Berner, 2003; Rogelj et al., 2018). However, there is an important lack of knowledge on how

90   weathering can contribute to climate change attenuation over a pluriannual timescale by

91   enhancing C storage through the entrapment of SOM within MOAs.

92   Mineral weathering has long been conceived as a very slow process leading to the genesis

93   of the soil profile over several thousands of years. In this view, soil minerals are considered

94   as stable phases and as soil intrinsic characteristics. Mineral properties are assumed to

95   influence their ability to protect SOM (Barré et al., 2014). Rasmussen et al. (2018) notably

96   demonstrated that oxyhydroxides, short-range-order minerals and phyllosilicates are of

97   particular importance in predicting SOM content, and that their relative importance in SOM

98   storage varies among soils as a function of soil acidity. In particular, phyllosilicates have

99   been proposed to dominantly contribute to SOM storage in neutral to basic soils through Ca^{2+}

100   mediation (Rowley et al., 2018; Rasmussen et al., 2018). Nevertheless, it was recently

101   demonstrated that the characteristics of minerals in soil can vary over very short timescales,

102   annually or even seasonally particularly due to biological activity (Turpault et al., 2007; Barré

103   et al., 2008; Collignon et al., 2012; Mareschal et al., 2013; Basile-Doelsch et al., 2015). In

104   nutrient-poor ecosystems such as forest ecosystems, minerals represent an important source

105   of nutrients for vascular plants and their associated microbiota (Ranger and Turpault, 1999;

4

106 Likens, 2013). They jointly operate to enhance the dissolution of minerals and the release of

107 the nutrients required to meet their respective needs, such as protons, organic acids and

108 metal chelatants (Hinsinger et al., 1992; Berner, 2003; Calvaruso et al., 2006; Courty et al.,

109 2010; Bonneville et al., 2011; Smits and Wallander, 2017; Finlay et al., 2020). Weathering

110 intensification by biological activity mainly occurs in the rhizosphere (Turpault et al., 2009)

111 and in the topsoil notably just below the forest floor in forest ecosystems (Augusto et al.,

112 2000). One may wonder if the intense weathering process undergone by phyllosilicates in the

113 above mentioned acidic conditions (Turpault et al., 2009) can contribute to carbon storage at

114 a pluriannual timescale.

115 Weathering encompasses different types of chemical and physical modifications of minerals:

116 dissolution of mineral constituents, mineral transformation (e.g., oxidation, cation exchange,

117 interlayer evolution) and mineral division. All of these processes can contribute to enhance

118 carbon storage, by producing fresh mineral surfaces accessible to organic moieties

119 adsorption, by changing the surface reactivity or by causing the formation of spaces where

120 organic matter can be trapped (Keil and Mayer, 2014). Most of the studies on SOM

121 adsorption onto phyllosilicate surfaces have focused on external surfaces (e.g. Newcomb et

122 al., 2017; Kleber et al., 2021). Nevertheless, SOM association inside phyllosilicate particles

123 could also be a potential stabilization mechanism, despite scarce field evidence (Kleber et

124 al., 2015).The weathering of phyllosilicates has some specificities due to their particular

125 structure. For example, 2:1 phyllosilicates are composed of one octahedral sheet, occupied

126 by cations such as Mg^{2+}, Fe^{3+} and Al^{3+}, between two tetrahedral sheets occupied by Si^{4+} and

127 Al^{3+} cations. The valence of the structural cations in the sheets creates net permanent

128 negative charges, which could be compensated by exchangeable cations in the interlayer.

129 Chemical weathering generally begins at the edge of sheets or in place of natural

130 defects, and propagates along the sheets toward the inner particles (Turpault and Trotignon,

131 1994). Interlayer cations are first released by dissolution or cation exchange (such as during

132 the transformation of mica into vermiculite in soil when the interlayer K is replaced by

133 hydrated exchangeable cations (Dixon and Weed, 1989; Barton, 2002). As weathering

progresses, dissolution processes solubilize the octahedral, followed by tetrahedral sheets. This creates empty spaces in the place of the solubilized mineral constituents, which are named exfoliation spaces. Physical weathering provoked by freeze/thaw events and mechanical pressure exerted by fungal hyphae can also generate exfoliation spaces in phyllosilicates by separating sheets and expanding the phyllosilicate structure (Wilson, 1966; Bisdom et al., 1982; Romero et al., 1992).

Additionally, weathering induces mineral neoformation by the precipitation of the elements present in soil solution, including cations released by mineral dissolution (Dixon and Weed, 1989; Romero et al., 1992). These secondary minerals encompass phyllosilicates, crystallized metal oxyhydroxides and short-range-order minerals (oxyhydroxides or aluminosilicates) (eg., Kleber et al., 2015). They are characterized by a large surface exposed to the soil solution and a high reactivity which contribute to their high potential to store organic matter. Precipitation of secondary minerals possibly occurs along with organic moieties. This process is responsible for the formation of nano-sized and poorly crystalline MOAs (Eusterhues et al., 2008; Basile-Doelsch et al., 2015; Tamrat et al., 2018, 2019), which may deposit onto weathered mineral surfaces. Coprecipitation creates spatial inaccessibility of entrapped organic compounds for soil microbes (Stockmann et al., 2013; Chenu et al., 2014; Keiluweit et al., 2017).

The approaches conducted thus far in the literature are not satisfactory for studying the impact of weathering on organic C trapping at a pluriannual timescale. Indeed, most existing studies on MOAs have analyzed simplified systems in laboratory-controlled conditions (Eusterhues et al., 2008, 2011; Mikutta, 2011; Mikutta et al., 2014). These experiments under artificial conditions do not completely reflect the functioning of an ecosystem, where multiple mechanisms drive MOAs formation. Some *in situ* investigations have been performed, taking advantage of soil chronosequences (Eusterhues et al., 2003; Mikutta et al., 2005, 2019; Doetterl et al., 2018), but it is difficult to deconvolve past and recent weathering processes and to know when C became associated with weathered minerals. The incubation of mineral bags is an approach traditionally used to quantify the nutrients released during mineral

162 weathering (Wallander and Wickman, 1999; Augusto et al., 2000; Turpault et al., 2009). It

163 offers an alternative to resolve this methodological gap and to investigate whether the initial

164 stages of mineral weathering are responsible for C sequestration within mineral organic

165 assemblages at the pluriannual timescale.

166 In this study, we investigated the contribution of the initial and recent stages of primary

167 phyllosilicate weathering to C storage using a unique mineral bag incubation experiment

168 performed over 20 years in the acidic soil of a temperate forest, just below the forest floor.

169 We hypothesized that large phyllosilicates also play an unaccounted role in SOM storage in

170 acidic soil, where low pH promotes weathering and enhances MOAs formation.

171 To test this hypothesis, we characterized the chemical and physical features of large (200-

172 400 µm) vermiculite particles incubated *in situ* for 20 years. We notably quantified their

173 carbon content and established their weathering budget. We also performed microscale

174 imaging investigations on the particle outer- and inner-surfaces using scanning electronic

175 microscopy (SEM) coupled with energy dispersive spectroscopy (EDS) searching for

176 potential C occurrence. We complementarily applied transmission electronic microscopy

177 (TEM) coupled with EDS and electron energy loss spectroscopy (EELS) on a focused ion

178 beam (FIB) section exposing the very inside of a weathered vermiculite particle to spatially

179 resolve the nature and chemistry of MOA at the nanoscale.

180 2 Material and Methods

181 2.1 Material

182 2.1.1 Site description

183 The experimental site was situated in a Douglas-fir (*Pseudotsuga menziesii*) ecosystem, in

184 the Beaujolais Hills in France (46° 10' N – 4° 38' E). The altitude was approximately 750 m

185 and the climate was characterized by a mean annual temperature of 11.8 °C and a mean

annual precipitation of 860 mm (1981-2010 period, Météo France). The Douglas-fir stand was planted in 1930 on an abandoned cropland (Ranger et al., 1997). In 1998, the stand was clear cut and replanted with the same species in 1999.

The soil was an Alocrisol (AFES, 1992) or dystric Cambisol (WRB) characterized by a moder humus type with OL, OF and OH layers (Ranger et al., 1997; Ezzaïm et al., 1999b). It developed from metamorphic volcanic tuff dating from the upper Visean (Ezzaïm et al., 1999a). This bedrock is composed of approximately 45% of phenocrysts - quartz, andesine, albite and biotite - and 55% of a matrix devitrified during metamorphism containing spherolites of quartz, K-feldspar, albite and andesine (Ezzaïm et al., 1999a, b). Bedrock weathering processes responsible for soil formation were mainly characterized by the transformation of biotite into Al hydroxy-interlayered vermiculite (Ezzaïm et al., 1999a).

The soil had a sandy-loam texture with a clay content varying from 20 to 25% (Table 1) and exhibited a high stone content (20 to 50% depending on the soil horizons) (Ranger et al., 1997; Ezzaïm et al., 1999a). It was acidic (pH_w ranging from 3.8 in the OL horizon to 4.3-4.6 in the mineral soil) and strongly desaturated (Table 1). The cation exchange capacity (CEC) decreased with depth from 8.7 $cmol_c$ kg^{-1} in the A1/Ap horizon to 4.5 $cmol_c$ kg^{-1} in the B1 horizon. Exchangeable Al occupied most cation exchange capacity with values ranging from 7.52 to 4.08 $cmol_c$ kg^{-1} (Table 1). Base saturation (BC/CEC) was 7.7 % in the A1/Ap horizon and 5.4 % in the B1 horizon, with the major base cations being K, Ca and Mg (Table 1). Al_{AO} extracted by ammonium oxalate decreased with depth from 6.2 to 3.3 $mg.g^{-1}$. Fe_{DCB} extracted by dithionite-citrate-bicarbonate was rather stable, varying from 9.3 in A1/Ap to 9.0 in B1 (Table 1). The organic carbon content decreased from 393 mg g^{-1} in the OL horizon to 251 mg in the combined fragmented and humified horizons (OF+OH) (Table 1). It decreased along the mineral soil profile from 47 mg g^{-1} in topsoil to 7 mg g^{-1} in the deepest horizon. The C/N ratio also decreased over the entire soil profile, from 36 in OL and 23 (OF+OH) to a value close to 11 in mineral soil. Total Ca decreased from organic to mineral horizons from

212 6.8 mg g^{-1} to 0.6 mg g^{-1}, respectively contrary to Mg and K, which increased with depth from

213 0.5 to 6.2 mg g^{-1} and from 1.3 to 34.8 mg g^{-1}, respectively (Table 1).

2.1.2 Mineral Material

215 A high-charge trioctaedric vermiculite from Santa Olalla (Andalusia, Spain) previously

216 described by de la Calle Vian (1977) and Augusto et al. (2001) was used in this study. This

217 contact metamorphic vermiculite satisfied the conditions required to study the impact of

218 primary phyllosilicate weathering on C storage: (i) it was a pure and homogeneous mineral,

219 (ii) it had a negligible amount of initial carbon, (iii) the particles size was larger than the bag

220 mesh size (20 microns to permit hyphae ingrowth but exclude root ingrowth). The structural

221 formula of the Na-saturated vermiculite was $((Si_{2.71} Al_{1.29}) (Mg_{2.52} Fe^{2+}_{0.02} Fe^{3+}_{0.24} Al_{0.12} Ti_{0.04})$

222 $Na_{0.97}O_{10} (OH)_2$ -Augusto et al., 2001)). This vermiculite was studied as a proxy for the

223 primary phyllosilicate of the studied site the parent material, which was biotite. The

224 vermiculite present in the soil profile was a product of the biotite weathering at its very early

225 stages, through the loss of interlayer K, and represented approximately 8% of the study soil

226 (Ezzaïm et al., 1999a).

2.2 Methods

2.2.1 Mineral-bags preparation, installation and collection

229 Santa Olalla vermiculite was prepared for *in situ* incubation in mineral-bags as follows.

230 Vermiculite particles, which size were between 200 and 400 μm in size, were saturated with

231 Na (1 M NaCl at 40 °C for 5 days (for more details see Augusto et al., 2001; Mareschal et al.,

232 2009)), because Na is an element that does not exist in the Santa Olalla vermiculite structure

233 and is low in acidic soils. Three grams of Na-saturated vermiculite and one gram of pure

234 quartz particles (250-400 μm) were placed into polyamide bags (n= 3, NYTREL TI polyamide;

235 10 cm x 5 cm and mesh size of 20 μm). Quartz particles were mixed with vermiculite to

facilitate soil solution percolation through the bag, and to prevent vermiculite particles from sticking together. Three mineral-bags (V20I, V20 II and V20 III) were inserted horizontally between the forest floor and mineral soil in fall 1997, and carefully protected during the Douglas fir harvest and replanting in 1998-99. The remaining, not-incubated, Santa Olalla vermiculite was used as a control for later comparison. Mineral bags were collected in 2017 after 20 years of *in situ* incubation. They were then dried at air temperature. Vermiculite particles were magnetically separated from the quartz particles. Then, samples were placed on a 30° inclined surface, which was submitted to manual vibration to remove soil particles that entered the mineral bags during the incubation. Indeed because of their round form, soil particles rolled more rapidly down the surface than the planar vermiculite particles. The few soil particles remaining on the inclined surface were finally handpicked. The quality of the separation process was checked through careful observation with binoculars.

2.2.2 Exchangeable cations and CEC analysis

Exchangeable cations were extracted from the vermiculite samples using either 1 M KCl for Na^+, Ca^{2+}, Mg^{2+}, Mn^{2+} and Fe^{3+} assays or 1 M NH_4Cl for K^+. Exchangeable cations were determined by inductively coupled plasma atomic emission spectrometry (ICP-AES, Jobin-Yvon JY38 Plus). The 1 M KCl vermiculite extract was also titrated with an automatic titrimeter (Mettler TS2DL25) to estimate exchangeable protons and exchangeable Al (Rouiller et al., 1980). The cation exchange capacity (CEC) was calculated as the sum of all exchangeable cations.

2.2.3 X-ray Diffraction (XRD)

X-ray diffraction (XRD) analysis was performed on control and weathered vermiculite samples as follows. An aliquot of the vermiculite samples was first K-saturated using a 1 M KCl solution. K saturated vermiculite particles were then exposed to the following sequential heating treatments: 110, 330 and 550 °C, each for a 4 hour period in an oven. This

procedure enabled the detection of hydroxylated interlayers by XRD. Mineralogical analysis of oriented vermiculite particles was determined by XRD using a Siemens D5000 diffractometer (Siemens Corp., New York, NY), equipped with a graphite monochromator and a Cu tube (Cu-Kα radiation) operating at 30 mA and 40 kV. Diffractograms were recorded using a DACO-MP recorder associated with a microcomputer using Diffrac AT software (Socabim, Champs-Sur Marne, France).

2.2.4 Total element chemical analysis

For elemental oxide analysis, 100 mg vermiculite was ground in an agate mortar. The sample was dried at 105 °C, fused with $LiBO_2$ and mineralized in 1 N HNO_3. The mineralized samples were then analyzed by ICP-OES (ICP-OES iCap6500 at the SARM laboratory, Nancy, France) to determine the elemental oxide composition (SiO_2, Al_2O_3, Fe_2O_3, MnO, MgO, CaO, Na_2O, K_2O and TiO_2). The associated uncertainty was <2% for SiO_2, Al_2O_3, MgO, <5% for Na_2O, <20% for MnO, <10% for Fe_2O_3, and <25% for CaO, K_2O and TiO_2. The procedure was replicated four times for each 20 year vermiculite mineral bag (V20 I, V20 II and V20 III) and for the control vermiculite sample (V0).

For organic C analysis, 30 mg vermiculite was ground in an agate mortar. Samples were analyzed for total C content by an elemental analyzer (Vario ISOTOPE cube, Elementar, Hanau, Germany), with a C detection limit of 0.1 mg g^{-1} and a C quantification limit of 0.3 mg g^{-1} (associated uncertainty was 0.05%). The procedure was performed in triplicate for each 20-year vermiculite mineral bag (V20 I, V20 II and V20 III) and for the control vermiculite sample.

2.2.5 Scanning Electron Microscopy

A dozen control vermiculite and 20-year weathered vermiculite particles were randomly selected for scanning electron microscopy (SEM) analysis. Among them, several 20 year weathered vermiculite particles, that exhibited a black deposit (manganese precipitate)

between the mineral layers, were longitudinally cut to expose the black material on their inner

surface. All particles were fixed onto a SEM holder with a silver lacquer. Most particles were

observed and analyzed without coating using a TESCAN VEGA 3 SEM equipped with energy

dispersive spectroscopy (EDS) (BRUKER) and with a silicon drift detector. Some particles

coated with graphite were observed and analyzed using a Hitachi S-4800 SEM equipped with

EDS and containing a lithium-drifted silicon detector, for the better sensitivity of this SEM to

image weathering marks. SEM EDS analyses were performed with an acceleration voltage of

15 kV and a working distance of 15 mm. The images were acquired with a BackScattered

Electron (BSE) and Secondary Electron (SE) detectors.

2.2.6 Focused Ion Beam

Two focused ion beam (FIB) sections were prepared from one 20 year weathered vermiculite

particle (V20n) bearing a manganese precipitate, which was longitudinally cut to expose the

black deposit on its inner surface. This particle was previously analyzed by SEM-EDS. Two

other FIB sections were prepared from a control vermiculite particle (V0) randomly selected.

A FIB/SEM Helios Nanolab 600i system with a gallium source was used to mill sections. The

particles were first sputter coated with platinum (~100 nm). The FIB instrument was operated

at 30 kV and 5 kV, and at beam currents between 1.40 and 0.17 nA. The produced sections

(V20n and V0n, respectively) had an 80 nm thickness.

2.2.7 Transmission Electron Microscopy

All FIB sections were examined with a JEOL ARM Cold FEG 200F transmission electron

microscope (TEM) operating at 200 kV and equipped with a spherical aberration Cs probe

and image correctors in an environment cooled at -170 °C using liquid nitrogen. Images were

acquired in TEM and scanning transmission electron microscopy (STEM) modes.

Measurements of interplanar spacing of the vermiculite were performed with electron

diffraction. Some regions of interest (ROIs) were defined for EDS analysis by determining the

area where a minimum of 1000 counts threshold was reached. EDS analyses were then

312 performed on the selected ROIs in STEM mode with a 0.5 nm diameter probe, using a Jeol

313 Centurio Silicon Drift Detector (SDD). Illumination conditions and acquisition parameters

314 (scanning vs. imaging mode, spot size, condenser aperture, convergence angle, time

315 constant, and integration time) varied with the size of the ROI and were adjusted to optimize

316 counting statistics.

317 The composition quantification of the collected EDS spectra was performed using the Cliff-

318 Lorimer method by dedicated software from Jeol, where the k-factors were determined using

319 the total elemental composition of the control vermiculite (V0). EDS data were processed

320 with Noran System Six software, and individual EDS counts data were normalized by the

321 sum of the counts of all elements to eliminate the bias generated by the heterogeneous

322 thickness of the FIB. EELS spectra were recorded in diffraction mode using GIF Quatum ER

323 in energy ranges from 260 eV to 300 eV to assess the C-edge and 610 eV to 680 eV to

324 assess the Mn-L2,3 edge. The spectrometer was set to an energy dispersion of 0.1

325 eV/channel. The condenser aperture, spectrometer entrance, and camera length were 150

326 μm, 2.5 mm and 4 cm, respectively, leading to a collection half angle of 20 mrad and an

327 energy resolution of 1 eV measured at full width at half maximum (FWHM) of zero loss peak.

328 Spectra were collected in either image (converged beam) or STEM mode at 200 keV from

329 regions measuring 1 to 100 nm in diameter using 3–10 s acquisition times. Acquisition was

330 performed during the first few seconds to avoid beam damage (which was indicated by peak

331 shift during recording).

332 **2.2.8 Calculations and Statistical analysis**

333 To compute the part of each element occurring as exchangeable form, we converted the

334 amount of each exchangeable cation (expressed in $cmol_c.kg^{-1}$ - see Table 2) into oxides (wt

335 %), using the molar mass and the charge of each element.

336 We computed the weathering mass balance over 20 years of vermiculite incubation in soil for

337 each element.   Element were expressed in their oxide form, at the exception of C. The mass

338 balance was calculated according to an isotitanium approach as follows:

339

340
$$\Delta m_{ox_j} = \left[ox_j(V20) * \frac{TiO_2(V0)}{TiO_2(V20)} \right] - ox_j(V0)$$

341 With:

342 Δm_{ox_j} = mass variation (gain or loss) of oxide j

343 ox_j (V0) = oxide j mass in control vermiculite (V0)

344 ox_j (V20) = oxide j mass in weathered vermiculite (V20)

345 TiO_2 (V0) = TiO_2 mass in in control vermiculite (V0)

346 TiO_2 (V20) = TiO_2 mass in weathered vermiculite (V20)

347 Values are presented as the mean and standard deviation for exchangeable cations, CEC,

348 total chemical composition and TEM-EDS analysis. Shapiro-wilk test was performed on the

349 residuals revealing that TEM-EDS, exchangeable cations and total chemical composition

350 data were close to a normal distribution (p-values = 0.001, 0.005 and 0.0001, respectively).

351 As a high heteroscedasticity was detected in TEM-EDS, exchangeable cations and total

352 chemical composition (p-value of the Bartlett's test of homogeneity of variances = $8.6e^{-12}$,

353 $1.717e^{-09}$ and $9.017e^{-07}$, respectively). To test pairwise differences between chemical

354 compositions of control vermiculite and each individual zone of the weathered vermiculite

355 zones (TEM data, exchangeable cations total chemical composition) we used an Exact Two-

356 Sample Fisher-Pitman Permutation Test, where the variances are not necessarily assumed

357 to be equal.

358 To compare the differences in C content assessed by TEM-EDS between the different

359 mineral zones observed in the weathered vermiculite FIB section and the control vermiculite

360   we conducted a Permutational MANOVA. The dependent variable was the C content and the

361   fixed effects corresponded to each mineral zone variable.

362

3   Results

3.1   Exchangeable cations

The cation exchange capacity of vermiculite strongly decreased during the 20 year *in situ* weathering (from 178.1 $cmol_c$ kg^{-1} for the control vermiculite (V0) to 49.2 $cmol_c$ kg^{-1} for the 20 year weathered vermiculite (V20 - Table 2)). The main exchangeable cation in V0 was Na with 97.5% of the total CEC, due to the initial Na saturation treatment. After the incubation period in the forest soil the V20 samples were completely depleted in exchangeable Na and enriched in exchangeable K, Ca, Mg, Mn and Fe: 0.63%, 42.6%, 28.7%, 9.40% and 0.44% of total CEC respectively (Table 2). The exchange acidity increased (H and Al cations) from 0.6% to 18.3% (Table 2).

3.2   Total chemical analysis

Table 3 shows significant differences in the carbon and oxide concentrations between V0 and V20, except for TiO_2 and Al_2O_3 (Table 3). The V20 samples presented a variable chemical composition. In particular CaO and MnO were significantly higher in V20 I than in V20 II and III. Weathered vermiculite presented a significant C content increase of 0.5±0.10 wt % compared with the control. The other analyzed elements were either structural (occupying the center of the tetrahedrons and octahedrons of the vermiculite sheets), exchangeable (in the CEC, mostly in the interlayers) or both. Over 20 years of weathering, the most abundant mineral structural elements suffered a significant decrease: SiO_2 decreased from 40.1±0.6 % to 35.5±0.4 %, MgO from 24.6±0.3 % to 21.7±0.4 % and Fe_2O_3 from 4.94±0.06 % to 4.49±0.06 % in V0 and V20 respectively. *In situ* weathering also induced the appearance of K_2O (0.25±0.05 %) and a significant increase in oxide mass (CaO and MnO from 0.41±0.03 % and 0.13±0.00 % in V0 to 0.66±0.30 % and 0.52±0.15 % in V20, respectively). The conversion of exchangeable cations (Table 2) in mass oxides revealed that 84±14 % CaO, 30±4 % MnO and 6±2 % K_2O were in exchangeable cation form. The

388 decrease in total measured oxides (from 94% to 81 wt %) likely corresponded to an increase

389 in OH and H_2O and in carbonaceous moieties.

3.3 X-ray Diffraction (XRD)

391 Figure 1 shows XRD patterns of oriented vermiculite samples, with or without a specific

392 treatment (K-saturation and sequential heating at 110 °C, 330 °C and 550 °C). The V0 and

393 V20 samples exhibited differences in d-spacing distance, which corresponded to the sum of

394 TOT width and interlayer space. Na-saturated V0 had a distance of 1.19 nm, which may

395 indicate the presence of one H_2O sheet in the interlayer. After 20 years of incubation, V20

396 showed a distance of 1.40 nm, suggesting interlayer opening. An interlayer collapse at 1.02

397 nm after K saturation was observed without heating in V0, whereas it progressively occurred

398 only after heating for V20, from 1.31 nm at 110 °C to 1.06 nm at 330 °C. This observation

399 suggests that weathering induced the formation of interlayer components in vermiculite that

400 were only removable by heating (Figure 1).

3.4 Binoculars

402 The observation of the V0 under the binocular loupe showed individual translucent particles,

403 variable in their color, from colorless to yellowish, with pearly luster. The V20 particles were

404 more opaque, presenting white to pale brown coloration and dull luster. Some of the V20

405 particles exhibited dark deposits on their outer-surfaces as well as between the mineral layer

406 stacks, interpreted as secondary mineral deposits.

3.5 Scanning Electron Microscopy

408 Figure 2 shows SEM images of the V0 and V20 outer- and inner-surfaces (after cutting along

409 the 001 plane). The V0 outer-surfaces presented a flat and smooth surface morphology

410 (Figure 2a and b). Scanning electron microscopy with energy dispersive spectroscopy (SEM-

411 EDS) detected no C on V0 outer-surfaces. In contrast the V20 particles were irregular and

marked by multiple cracks of chemical dissolution on their outer surfaces (Figure 2c, d and e) and lighter dissolution features on their inner surfaces (Figure 2k and l). The whiter zones in the SEM-BSE images (Figure 2g, h, k and l) corresponded to the dark deposits onto V20 observed with the binoculars. These secondary mineral deposits were mainly enriched in Mn, but also in Fe, Ca and C, as revealed by the EDS spectrum (Figure 2i). C was detected on all weathered particle outer surfaces but especially in the darker zones of SEM-BSE images (Figure 2e, g, f and h). In Figure 2e the darker zones could correspond to the presence of hyphae. In Figure 2g, C was detected in the Mn deposits. On V20 outer surfaces we found Ca-rich deposits (Figure 2f and j) that could correspond to oxalate crystals according to morphological similitudes with Krieger et al (2017). The V20 inner surfaces exhibited the same Mn-, Fe-, Ca- and C-rich depositions, which appeared white in the SEM-BSE images (Figure 2k and l) as those found on the particle outer surfaces. C was also detected in the darker gray zones of the depositions (Figure 2k and l).

3.6 Transmission Electron Microscopy

3.6.1 Control vermiculite ultrathin section (V0)

The TEM image of the ultrathin section extracted from the control vermiculite particle V0 (V0n) showed a sheet structure without any weathering marks (Figure 3a). The electronic diffraction pattern (Figure 3b) indicated a crystalline structure with a d-spacing of 1 nm, which is typical of dehydrated vermiculite, probably due to the intense TEM vacuum (Murakami et al., 2002). The chemical maps revealed a homogeneous chemical composition (Figures 3c to 3h) and the same stoichiometry as observed at the macroscale (Table 3 and Table 4).

3.6.2 Weathering trends

Unlike the control vermiculite particles, the 20-year weathered vermiculite was heterogeneous at the nanoscale and exhibited various forms of physicochemical weathering (Figure 4), particularly some nanoscale and microscale exfoliation spaces, whose orientation

18

437   was parallel to the vermiculite sheets. Chemical maps revealed that the mineral matrix of the

438   weathered particle exhibited typical characteristics of slightly altered vermiculite minerals

439   (zone called V20n in Table 4). It was completely Na depleted and mainly composed of Si and

440   Al. Its elemental composition was significantly different from that of the control vermiculite,

441   except for the C and K contents. (Table 4). The nanoscale exfoliation spaces observed in the

442   mineral matrix of the 20-year weathered vermiculite were 9 to 90 nm wide. Most of them

443   were filled with a material enriched in C compared with the control vermiculite, either in

444   association with Si enrichment (ES Si - Table 4, Figure 5 black arrows in top row) or in

445   association with Ca enrichment (ES Ca - Table 4, gray arrows in Figure 5 bottom row). The

446   absence of oxygen detection in any of these C-rich exfoliation spaces excluded carbonate-

447   like compounds and pointed to the presence of organic matter.

448   Two large, microscale, exfoliation spaces were also observed in the mineral matrix of the 20

449   year weathered vermiculite. Their widths varied along the FIB section from 0.7 to 2.4 μm

450   (Figure 4b). Chemical maps showed that they were filled with distinct secondary mineral

451   assemblages: either Mn-enriched deposits (Mn oxide - Figures 6 and 7) or Si- and Al-

452   enriched (noted SiAl) and Si-, Al- and K-enriched (noted SiAlK) precipitates (Figure 7). The

453   Mn oxide exhibited a petrographic morphology that followed the same orientation as the

454   V20n sheets, suggesting a deposit on one inner surface delimiting the microscale exfoliation

455   space. Electronic diffraction analyses indicated differences in the crystallization degree

456   depending on the spatial scale that they were performed at. Mn oxide deposits appeared

457   amorphous at a 50 nm scale, while a crystalline diffraction pattern was detected at a 5 nm

458   scale (Figure 6a and 6b, respectively). The d-spacing measurements by electronic diffraction

459   (Figure 6b) were typical of the $Mn(II)Mn(III)_2O_4$ form, commonly known as hausmannite

460   (Chukhrov and Gorshkov, 1981). EELS analysis indicated that Mn was present as Mn(II) and

461   Mn(III), as in hausmannite (peaks at 642 and 653 eV, respectively) (Figure 6 c). Mn oxide

462   was colocalized with Fe, Ca, and C (Figure 6a right), and all these elements were

463   significantly more concentrated in the weathered vermiculites than in the control vermiculite

464   (Table 4). The C-rich zones were located around the hausmannite nanocrystal zones (Figure

465   6 a). STEM-EDS mapping revealed the presence of a zone dominated by Si and Al between

466   the hausmannite deposit and the mineral matrix of the altered vermiculite (Figure 7), which

467   shows a higher chemical variability than the other zones (Table 4). We identified two mineral

468   poles: (i) SiAl and (ii) SiAlK. The chemical composition of the silicate-like pole – SiAl, was

469   very similar to the chemical composition of kaolinite present in the soil profile of the study site

470   (see Ezzaïm et al., 1999a, b). Both aluminosilicate assemblages (SiAl and SiAlK) presented

471   an unorganized morphological configuration that suggested secondary mineral neoformation

472   by precipitation in the microscale exfoliation space.

473   **3.6.3 Characteristics of the organic matter associated to the weathered**

474   **vermiculite**

475   The weathering processes enabled the formation of several MOAs significantly enriched in

476   carbon compared with the control vermiculite. Mineral-associated organic matter was

477   significantly concentrated in the nanoscale exfoliation spaces, in the Mn oxide zone and in

478   the SiAlK zone, the latter two observed in the microscale exfoliation spaces (Figure 8). These

479   MOAs were also characterized by a high content in base cations: Ca, or K for the SiAlK zone

480   (Table 4).

481   TEM-EELS analyses were performed on the control vermiculite FIB section and on two

482   regions of interest of the weathered vermiculite particle FIB section: the nanoscale exfoliation

483   spaces enriched in Ca and C and on the Mn oxide. We did not detect any significant signal of

484   C speciation in the control vermiculite FIB section, but observed marked differences in C

485   speciation between small exfoliation spaces and Mn oxide (Figure 9). In the nanoscale

486   exfoliation spaces enriched in Ca we identified alcohol or carboxyl functional groups at 289

487   eV and C=C bond resonance at 292 eV (Figure 9) (Braun et al., 2005; Solomon et al., 2012).

488   In the Mn oxide deposit the first peak at 287 eV may be assigned to a variety of organic

489   moieties: aliphatic, aromatic, or carbonyl moieties (Braun et al., 2005). The peak at 290 eV

490   could be assigned to the carboxylic acid (Solomon et al., 2012) (Figure 9).

491   # 4   Discussion

492   ## 4.1   Mineral bags as an alternative method to study MOA formation

493   Until now the role of weathering in the associations of organic matter to mineral phases has

494   been studied using soil chronosequences or laboratory experiments. Soil chronosequences

495   typically expand over centennial (e.g., Vermeire, 2017; Doetterl et al., 2018) to pluri-millennial

496   timescales (Mikutta et al., 2009, 2019). They are observed after glacier retreat, on

497   successive volcanic lava, on river terraces or on advancing sand beach deposits. They have

498   permitted to investigate *in situ* the changing nature of mineral organic associations during the

499   parent material weathering process. However, as they integrate a multiplicity of weathering

500   processes, it is impossible to isolate any individual one in order to understand how organic

501   matter becomes associated to weathered minerals.

502   In contrast laboratory experiments have been designed to understand specific processes. It

503   should be noted that while information on the association of organic matter with secondary

504   minerals is abundant, information on the association of organic matter with primary mineral

505   submitted to weathering is lacking. Laboratory experiments have examined how organic

506   matter association with secondary minerals is dependent on soil conditions such as solution

507   pH, elements in solution and their concentration, organic matter amount and speciation, etc.

508   (see the review by Kleber et al. (2015) for details about MOAs drivers). Information about the

509   intimate spatial organization of organic and mineral components has been obtained through

510   the development of nanoscale imaging and spectroscopic techniques (i.e., Eusterhues et al.,

511   2008; Estes et al., 2017; Newcomb et al., 2017). Nevertheless, one major drawback of

512   laboratory experiments is the simplification of the studied system, while the functioning of a

513   soil is driven by multiple factors. Often only the abiotic chemical weathering is reproduced,

514   while the physical weathering is forgotten, as well as the biological weathering (i.e. plant and

microbe functioning, which contribute directly to the alteration of minerals, and indirectly by recycling of elements in the ecosystem). Moreover, the conditions of chemical weathering are only partially reproduced and do not take into account the spatio-temporal dynamics of weathering in soil (i.e. soil structuration in pedogenic horizons, aggregation, seasonal changes induced by biology and climate). Finally, laboratory experiments are carried out over daily to annually timescale, which prevents to account for any dynamic interactions occurring between minerals and organic matter such as enhanced or reduced weathering/decomposition (e.g. Kleber et al., 2021; Li et al., 2021b).

In contrast, the mineral bag experiment offers a unique opportunity to bridges the knowledge gap between laboratory studies and soil chronosequence studies as it examines the incipient weathering reactions and subsequent carbon sequestration over a pluriannual to pluridecadal timescale. It also advantageously investigates processes in a real complex and dynamic soil system. Another benefit of this technique is the possibility to study the C storage in both the altered the primary minerals and the newly formed secondary minerals deposited on the primary mineral surfaces.

4.2 Vermiculite weathering processes occurring over 20 years

After 20 years of weathering under the forest floor, the Na saturated vermiculite particles presented pronounced dissolution marks on their outer-surfaces and lighter dissolution traits on their inner-surfaces (Figure 2). One possible reason for the apparent lower sheet dissolution inside the particle is that the dissolution of phyllosilicate sheets mostly affects mineral edges and basal outer-surfaces, as observed by Turpault and Trotignon (1994), Nagy (1995), Kalinowski and Schweda (2007) and Bray et al. (2015). This process generates edge defects that can result in net surface charge increase and reactivity (Turpault and Trotignon, 1994; Bickmore et al., 2001).

A weathering balance was calculated according to Equation 1. Na was completely depleted from V20. SiO_2, Fe_2O_3 and MgO, the main components of the vermiculite tetrahedral and

542 octahedral sheets were released nearly stoichiometrically: 3.97 g, 0.38 g and 2.47 g,

543 respectively, per 100 g of control vermiculite (Figure 10). This corresponds to an

544 approximately 10% loss of these structural components (Table 3). We thus assumed that

545 10% of structural Al was also dissolved (i.e. about 1.76 g of Al_2O_3 for 100 g of initial

546 vermiculite). On the other hand, the weathering mass balance showed an overall mass gain

547 due to Al_2O_3, CaO, K_2O and MnO inputs of 0.18 g, 0.26 g, 0.26 g and 0.40 g, respectively per

548 100 g of control vermiculite and to the sequestration of 0.5 g of C per 100 g of control

549 vermiculite (Figure 10).

550 A typical pattern of Santa Olalla vermiculite weathering is the precipitation of Al hydroxides in

551 the interlayer, which replace other cations at the reactive sites in the interlayer, accompanied

552 by a reduction of exchange sites (Augusto et al., 2001; Mareschal et al., 2009). Several of

553 our observations indicated that this interlayer hydroxylation occurred within 20 years of *in situ*

554 incubation. (i) The observed strong CEC decrease (178.1 to 49.2 cmol$_c$ kg^{-1}) was associated

555 with a blockage of the mineral exchange sites in the interlayer. (ii) The interlayer noncollapse

556 after K saturation and its partial collapse with heating at 330 °C (Figure 1) are typical features

557 of vermiculite interlayer hydroxylation (Dixon and Jackson, 1959; Ezzaïm et al., 1999a) and

558 in particular about the Santa Olalla vermiculite: (Ranger et al., 1991; Augusto and Ranger,

559 2001; Mareschal et al., 2009; Lanson et al., 2015). (iii) The moderately acidic soil solution

560 (pH 4.8) was optimal for Al hydroxy-interlayer formation (Rich, 1968). Accordingly, vermiculite

561 minerals, which were originally present in the soil of the study site, also exhibited interlayer Al

562 hydroxylation (Ezzaïm et al., 1999a). Al hydroxy-interlayer mainly derived from the

563 vermiculite congruent sheet dissolution (1.76 g released by congruent vermiculite dissolution

564 against 0.18 g deriving from external sources of Al_2O_3, as mentioned earlier – see Figure 10).

565 It is likely that the maximum Al hydroxylation was reached within 20 years of *in situ*

566 incubation, blocking CEC at 50 cmol$_c$ kg^{-1} (Table 2), which was the minimum CEC threshold

567 observed with increasing weathering by Augusto et al. (2001) and Mareschal et al. (2009)

568 regarding *in situ* and laboratory experiments, respectively, on the same Santa Olalla

569 vermiculite.

570   The interlayer exchange sites were not totally blocked by Al hydroxy but was occupied by

571   other cations, Ca, Mg, Mn and K, which replaced the exchangeable Na in the control

572   vermiculite (Table 2). They were derived from the dissolution of mineral sheets (i.e. Mg) or

573   came from external sources such as the decaying litter and soil solution (i.e. Mn, Ca and K –

574   Figure 10), as also observed by Augusto et al. (2001).

575   The nanoscale and microscale exfoliation spaces formed along the stacking direction found

576   in V20 (Figures 4, 5 and 7) have often been described in the literature (Wilson, 1966; Bisdom

577   et al., 1982; Romero et al., 1992; Turpault and Trotignon, 1994; Jeong, 1998; Gillot et al.,

578   2000; Balassone et al., 2017), but were never related to change in C storage. These authors

579   suggested that exfoliation was caused by chemical dissolution and physical breakdown along

580   the 001 plane orientation, starting at the sheet edges and followed by the propagation of the

581   alteration front along the sheets. Exfoliation is known to be initially induced by ion interlayer

582   exchange (Romero et al., 1992). It is also likely that exfoliation space formation was

583   associated with physicochemical weathering, induced by freezing and thawing, along with the

584   sheet dissolution induced by protons and organic cations in soil solution, as observed for

585   smectite by Keil and Mayer (2014). The initial nanoscale exfoliation spaces (Figure 5)

586   progressed until single stack individualization, resulting in almost complete exfoliation, i.e.,

587   partial separation of the sheets along the 001 planes, forming larger, microscale, exfoliation

588   spaces (Figures 4 and 7) (Romero et al., 1992; Keil and Mayer, 2014). This phenomenon

589   was often observed in thin sections of soil samples, where weathered phyllosilicates

590   presented secondary minerals, like oxyhydroxides, that were seen to precipitate inside the

591   exfoliation spaces (Wilson, 1966; Bisdom et al., 1982).

592   Secondary mineral precipitates were observed in the microscale exfoliation spaces, notably

593   deposits of Mn_3O_4 nanocrystals of 5 nm diameter, consistently with the Mn gain computed in

594   the weathering mass balance. The nanocrystals were identified as hausmannite (Figure 6b),

595   one of the most common forms of manganese oxide minerals in soil profiles (McKenzie,

596   1972), widely distributed in soils (Luo et al., 2018). We also observed some neoformed

597   secondary SiAl precipitates in the large exfoliation spaces (Figure 7), despite the absence of

598   direct evidence of the weathering balance (Figure 10). These SiAl were identified as

599   kaolinite, and their mineral composition was not significantly different from that of the

600   kaolinite present in the soil profile (data in Ezzaïm et al. (1999a, b)). Furthermore, the

601   precipitation of kaolinite in phyllosilicate openings during weathering has often been

602   observed in soils in a process called kaolinization (Wilson, 1966; Bisdom et al., 1982;

603   Banfield and Eggleton, 1988; Tan et al., 2017; Li et al., 2020a).

4.3 SOM storage in the weathered vermiculite particle over 20 years

604

605

4.3.1 No evidence of SOM in the interlayer of the weathered vermiculite

606

607   We did not detect significant C enrichment in the zone identified as the weathered vermiculite

608   matrix (V20n), while SOM intercalation in 1:2 phyllosilicate interlayers is considered a

609   potential SOM stabilization mechanism in natural soil. (Kleber et al., 2015). It has been

610   reported in laboratory experiments under strong chemical or thermal treatments for

611   phyllosilicates such as montmorillonite which are more expandable than vermiculite

612   ((Monvisade and Siriphannon, 2009; Hu et al., 2016). In the field, the scarce observations

613   performed so far are indirect deductions made from the interlayer collapse upon sample

614   heating up to 400°C, or after H_2O_2 treatment, and the simultaneous loss of SOM (e.g.,

615   Leinweber and Schulten, 1995; Skiba et al., 2011). Theoretically, penetration of SOM in

616   vermiculite interlayers could occur, in particular because Al hydroxy groups did not occupy all

617   the space but were distributed as 'islands' in the interlayer (Meunier, 2007). They kept the

618   interlayer open, but also blocked it at 0.4 nm, preventing larger expansion. The 0.4 nm

619   distance corresponds to the difference between d-spacing of Al hydroxy-interlayered

620   vermiculite and dehydrated vermiculite (Dixon and Weed, 1989). As a result if SOM

621   penetration in the Al hydroxy interlayers occurs, it would be limited to small organic cations,

622 which should be planar to fit into the 0.4 nm interlayer opening (Georgiadis et al., 2020).

623 These small organic cations would probably be too low-sized to be detected by the current

624 resolution of TEM-EELS technique.

4.3.2 SOM entrapped and chemically bound in nanoscale exfoliation spaces of weathered vermiculite

627 A novelty of our study is that we showed evidence that the physical alteration and chemical

628 dissolution of the phyllosilicate structure created spaces within the mineral particle that

629 played an important role in C storage. This role of exfoliation spaces formed between

630 coherent stacks of phyllosilicate in C storage has been largely overlooked until now, while

631 they may physically protect SOM from decomposer action (Nielsen, 1967; Alexandre and

632 Dubois, 2000; Bolton et al., 2006; Kiersnowski et al., 2009; Taghaddosi et al., 2017). Most

633 nanoscale exfoliation spaces were filled with C and jointly trapped with Ca (Table 4), and it is

634 likely that Ca played a role in SOM storage. Despite the acidic nature of the soil, non-

635 neglectable amounts of calcium (290 µmol L^{-1}) circulate in the soil solution and collected in

636 organic layers and in the first top centimeters of the topsoil at our experimental site

637 (Marques, 1996), and at other sites (e.g., Grand and Lavkulich, 2013).They are released by

638 intense biological recycling of Ca-rich biominerals as Ca oxalate- and Ca-rich organic

639 molecules (Dauer and Perakis, 2014; Krieger et al., 2017; Berg et al., 2017; Turpault et al.,

640 2019; Dincher et al., 2020). The organic moieties identified in the Ca-enriched nanoscale

641 exfoliation spaces possibly consisted of partly oxidized litter decomposition products in

642 accordance with the EELS peak at 289 eV (assigned to alcohol or carboxyl functional

643 groups) and aromatics in accordance with the with the C=C bond resonance at 292 eV

644 (Braun et al., 2005). The role of Ca in SOM stabilization is not well-known in acidic media,

645 where it has been dismissed until now in favor of investigations of SOM interactions with

646 metal oxides (Kleber et al., 2015; Rowley et al., 2018; Rasmussen et al., 2018). We suspect

647 that Ca promoted the assemblage between polar or negatively charged organic moieties and

648 negatively charged vermiculite sheets, possibly until a maximum surface loading as

649　suggested by Figure 11. Possible mechanisms include covalent bonding via cation bridging,

650　and weaker electrostatic bonding through cation-pi-donor interaction and water bridging

651　(Sposito, 2008; Keiluweit and Kleber, 2009; Kleber et al., 2015; Newcomb et al., 2017;

652　Rowley et al., 2018). Ca may not only be involved in SOM-mineral interactions, but may also

653　act as a bridging agent between different organic moieties filling the exfoliation spaces.

654　Multivalent cations such as Ca indeed suppress the electrostatic repulsion between polar or

655　negatively charged organic molecules and promote their cohesion through the Ca^{2+}-mediated

656　interactions previously mentioned (Mouvenchery et al., 2012). Molecular modeling also

657　indicates that Ca^{2+}-mediated molecular cross-links reduce the distance between molecules

658　(Aquino et al., 2011), which maximizes the C storage within the exfoliation space boundaries

659　until a threshold, as it could also be interpreted from the Figure 11. The crosslinking

660　established between organic compounds is supposed to retard their mineralization and

661　stabilize them (Mouvenchery et al., 2012). Ca-stabilized SOM would then accumulate in the

662　nanosized exfoliation spaces until they became completely filled.

4.3.3　Double physical protection of SOM: coprecipitated by Hausmannite and other secondary minerals found in microscale exfoliation spaces

665　In the large microscale exfoliation spaces, we observed the co-occurrence of organic C and

666　precipitated secondary minerals, identified as SiAlK and hausmannite Mn oxides. The

667　importance of occlusion in SOM storage has already been demonstrated, mainly with Mn and

668　Fe oxides (Johnson et al., 2015; Kleber et al., 2015 and references therein). Another novelty

669　of this study is the presence of SOM in the mineral precipitates, contained inside vermiculite

670　large exfoliation spaces, offering organic C a double physical protection. Additionally the high

671　content of Ca in the Mn-oxides zone (Figure 6, Table 4) suggests that this cation is involved

672　in the cohesion of organic matter within the precipitate, (Mouvenchery et al., 2012; Allard et

673　al., 2017; Newcomb et al., 2017), notably if it is constituted of carboxylic acids as suggested

674　by the EELS peaks. Ca may also be involved in cation bridging between SOM and the

675　hausmannite nanocrystals (if they are negatively charged). This latter possibility remains

hypothetical as the point of zero charge (PZC) of the hausmannite exhibits large variations in the literature as a function of the sample origin, synthesis, crystallinity, temperature and degree of hydration (Heitmann et al., 2016). Similarly, the presence of K in the C enriched aluminosilicate precipitates (Figure 9) suggests a role of K in SOM storage and its interaction with mineral surfaces, as observed by Lutfalla et al. (2019). This monovalent cation can indeed suppress the repulsion between negatively charged mineral surfaces and negatively charged organic matter according to the DLVO theory, but in a less efficient way than divalent cations (Stumm and Morgan, 1996). Taken together, these observations point out to an important role of cations in facilitating chemical interactions enhancing C storage during vermiculite weathering.

The hausmannite deposits appeared amorphous at the 50 nm scale. Such amorphous to poorly crystalline nanosized minerals coprecipitated with SOM have also been described by others at similar scales (e.g., Tamrat et al., 2019). However the downscaling to a 5 nm resolution unraveled the fine crystalline nanostructure of hausmannite (Figure 6b) and showed that the nanocrystals were surrounded by a matrix enriched in C (Figure 6a). According to what we found in hausmannite nanosized crystals, Eusterhues et al. (2008) also provided indirect visual and crystallographic evidence of SOM location around the 2-line ferrihydrite nanocrystal-organic matter coprecipitates at a fine scale (20 nm).

Weathering mass balance indicated that Mn mainly derived from an external source rather than from vermiculite dissolution (Figure 10). Mn is a critical micronutrient for plants, which is not translocated or reabsorbed during senescence and return to soil through litterfall (Li et al., 2021a). After release from decaying litter, it is transported down through the forest floor and circulates as dissolved Mn^{2+} or dissolved $Mn^{2+/3+}$ chelated by carboxylic acids in the soil porosity (what includes the microporosity of vermiculite exfoliation spaces).

The abiotic oxidation of Mn(II) at low pH is thermodynamically unfavorable, but some bacteria and fungi have been identified for their ability to oxidize Mn(II) at acidic conditions and to

702   sometimes induce a subsequent precipitation of Mn oxides (Qian et al., 2019; Zhou and Fu,

703   2020). Ivarson and Heringa (1972) notably observed the fungal induced precipitation of

704   hausmannite. Electron microscopy showed that the Mn oxides generated by microorganisms

705   varies in shape and size. They occur as coating on hyphae, as coating on soil particle or as

706   infill between mineral particles as in our study (Mayanna et al., 2015; Bohu et al., 2016;

707   Pinzari et al., 2018; Dincher et al., 2020). The biotically induced oxidation of Mn oxides

708   depends on enzymes, reactive oxygen species and organic acids such as oxalate. A well-

709   studied example is the lignin decomposition pathway operated by brown rot fungi (Hofrichter,

710   2002). These organic molecules secreted by microorganisms can circulate until a certain

711   distance to the producing organism, which may explain why we did not identify any form of

712   alive or dead microorganisms in our thin sections observed at the sub-nanometric scale.

713   It is suspected that the proteins and organic acids involved in Mn(II) oxidation may serve as

714   nucleation sites for unstable Mn(III) (Tang et al., 2013; Keiluweit et al., 2015; Pinzari et al.,

715   2016; Estes et al., 2017). This would be in accordance with the EELS observation in the Mn

716   oxide zone revealing an intense peak assigned to carboxylic acid (Figure 9), and consistent

717   with other OM spectra obtained in Mn oxides (Chorover and Amistadi, 2001; Johnson et al.,

718   2015; Estes et al., 2017; Allard et al., 2017). A substantial quantity of organic molecules may

719   have been harbored and sequestered during Mn oxide growth. However, the presence of

720   SOM in the hausmannite precipitates may have blocked Mn crystal growth at the nanocrystal

721   stage, as suggested by Eusterhues et al. (2008, 2014), Mikutta and Kretzschmar (2008) and

722   Cismasu et al. (2011).

723   The hausmannite nanocrystals displayed a high specific surface area and numerous reactive

724   sites for additional interaction with organic moieties, which could explain why Mn oxides

725   contained significantly more C than other regions located inside of the weathered vermiculite

726   (i.e., the exfoliation spaces, Table 4 and Figure 8). Assuming that positively charged Mn

727   oxides and carboxylates were the dominant species at microlocal pH conditions, strong

728   binding by surface ligand exchange mechanism may have been responsible for the observed

729   association as mentioned by Johnson et al.(2015) and Allard et al. (2017). Assuming that Mn

oxides are negatively charged, weaker binding between Mn oxides and carboxylates through surface Ca cation bridging may have occurred as well (Allard et al., 2017), similarly to what is called ternary complex in the case of iron oxides associated to OM (Fe-Ca-OM interaction) (Sowers et al., 2018).

4.3.4 About the fate of weathered vermiculite and its implication on C storage

Over 20 years of *in situ* weathering the initially C-free vermiculite particle has acted as a net C sink. C sink occurred both in the nanosized exfoliation spaces and within the Mn oxides coprecipitates. We suspect that the SOM trapped in the vermiculite nanosized exfoliation spaces and further chemically bond to mineral surfaces will be protected from decomposition over long time-scales. The Al hydroxyl groups, precipitated in the vermiculite interlayers, indeed stabilize the phyllosilicate structure and the organic matter reduces the access of weathering agents to the mineral matrix.

It can further be assumed that the organic matter tightly associated to the Mn oxides is also efficiently protected from decomposer activity through both chemical binding and physical entrapment. However, it is unclear whether occluded organic matter is protected from abiotic oxidative mineralization. Hausmannite indeed has the ability to oxidize organic matter, due to the presence of Mn(III) in its structure. Mn(III) reduction into Mn(II) contributes to organic matter degradation and induces the alteration of the Mn oxide structure and the release of soluble Mn^{2+} (Kung and McBride, 1988; Li et al., 2021a). Physical preservation and abiotic oxidation of Mn oxide-hosted carbon may thus occur within the same deposit (Johnson et al., 2015; Estes et al., 2017). However the circumstances of SOM abiotic degradation by Mn oxides are still largely unknown. Reardon et al. (2018) notably showed that it could be inhibited by a high concentration of carbohydrates.

Additionally, the 20-year weathered vermiculite particles likely offer additional potential for C storage in empty exfoliation spaces. The progression of weathering is expected to induce the

formation of new exfoliation spaces and novel secondary mineral-organic coprecipitates. We postulate that C storage increases until the weathering eventually induces the complete separation of the vermiculite sheets, which will eventually expose the organic matter to the soil solution and decomposing agents. But we expect that the weathering processes will slow down compared to those occurring during the first 20 years. Only a longer-term experiment could confirm this hypothesis.

Conclusion

In this study, the mineral bag incubation technique emerges as a successful methodology to provide new insights into the impact of *in situ* mineral weathering on carbon storage. This method brings new knowledge on processes occurring at the weathering initial stages and integrate the complexity of the biogeochemical functioning of soil. It enables the investigation over two decades of secondary minerals precipitation and of physico-chemical changes affecting the primary mineral matrix, which contribute both to C storage.

Fine-scale observations revealed that inner particle weathering processes promote the formation of nano- to micro-sized exfoliation spaces in large phyllosilicate where organic matter becomes entrapped, sometimes in association with secondary mineral deposits (i.e. Mn oxides). The entrapment of organic matter in exfoliation spaces and in Mn oxides coprecipitates contributes to its physical protection. The co-occurrence of cations such as Ca with the trapped organic matter further suggests enhanced chemically mediated stabilization.

Our observations performed after only two decades of vermiculite weathering in acidic soil challenge the common vision considering minerals as stable partners in mineral organic assemblages and call for closer consideration of the role of phyllosilicates in C storage in acidic soils.

780 Further fine-scale investigations are required to verify whether the new processes, identified

781 in this study, drive C storage inside phyllosilicates during weathering sporadically or are

782 generic to various soil horizons and pedogenetic environments, including vermiculite

783 utilization in crop farming. It is also crucial to explore for how long these processes contribute

784 to C stabilization.

5 Acknowledgments

797

6 References

Alexandre M. and Dubois P. (2000) Polymer-layered silicate nanocomposites: preparation, properties and uses of a new class of materials. *Materials Science and Engineering: R: Reports* **28**, 1–63.

Allard S., Gutierrez L., Fontaine C., Croué J.-P. and Gallard H. (2017) Organic matter interactions with natural manganese oxide and synthetic birnessite. *Science of The Total Environment* **583**, 487–495.

Aquino A. J., Tunega D., Schaumann G. E., Haberhauer G., Gerzabek M. H. and Lischka H. (2011) The functionality of cation bridges for binding polar groups in soil aggregates. *International Journal of Quantum Chemistry* **111**, 1531–1542.

Augusto L. and Ranger J. (2001) Experimental in situ transformation of vermiculites to study the weathering impact of tree species on the soil. *European Journal of Soil Science* **52(1)**, 81–92.

Augusto L., Ranger J., Turpault M. and Bonnaud P. (2001) Experimental in situ transformation of vermiculites to study the weathering impact of tree species on the soil. *European Journal of Soil Science* **52**, 81–92.

Augusto L., Turpault M.-P. and Ranger J. (2000) Impact of forest tree species on feldspar weathering rates. *Geoderma* **96**, 215–237.

Balassone G., Nieto F., Arfè G., Boni M. and Mondillo N. (2017) Zn-clay minerals in the Skorpion Zn nonsulfide deposit (Namibia): Identification and genetic clues revealed by HRTEM and AEM study. *Applied Clay Science* **150**, 309–322.

Banfield J. F. and Eggleton R. A. (1988) Transmission Electron Microscope Study of Biotite Weathering. *Clays and Clay Minerals* **36**, 47–60.

Barré P., Fernandez-Ugalde O., Virto I., Velde B. and Chenu C. (2014) Impact of phyllosilicate mineralogy on organic carbon stabilization in soils: incomplete knowledge and exciting prospects. *Geoderma* **235**, 382–395.

Barré P., Velde B., Fontaine C., Catel N. and Abbadie L. (2008) Which 2: 1 clay minerals are involved in the soil potassium reservoir? Insights from potassium addition or removal experiments on three temperate grassland soil clay assemblages. *Geoderma* **146**, 216–223.

Barton C. (2002) Clay minerals. *In: Rattan Lal, comp., ed. Encyclopedia of Soil Science. New York, New York: Marcel Dekker: 187-192.*

Basile-Doelsch I., Balesdent J. and Pellerin S. (2020) Reviews and syntheses: The mechanisms underlying carbon storage in soil. *Biogeosciences* **17**, 5223–5242.

Basile-Doelsch I., Balesdent J. and Rose J. (2015) Are Interactions between Organic Compounds and Nanoscale Weathering Minerals the Key Drivers of Carbon Storage in Soils? *Environ. Sci. Technol.* **49**, 3997–3998.

835 Berg B., Johansson M.-B., Liu C., Faituri M., Sanborn P., Vesterdal L., Ni X., Hansen K. and
836   Ukonmaanaho L. (2017) Calcium in decomposing foliar litter – A synthesis for boreal
837   and temperate coniferous forests. *Forest Ecology and Management* **403**, 137–144.

838 Berner R. A. (2003) The long-term carbon cycle, fossil fuels and atmospheric composition.
839   *Nature* **426**, 323–326.

840 Bickmore B. R., Bosbach D., Hochella M. F., Charlet L. and Rufe E. (2001) In situ atomic
841   force microscopy study of hectorite and nontronite dissolution: Implications for
842   phyllosilicate edge surface structures and dissolution mechanisms. *American
843   Mineralogist* **86**, 411–423.

844 Bisdom E., Stoops G., Delvigne J., Curmi P. and Altemuller H.-J. (1982) Micromorphology of
845   weathering biotite and its secondary products. *Pedologie* **32**, 225–252.

846 Bohu T., Akob D. M., Abratis M., Lazar C. S. and Küsel K. (2016) Biological low-pH Mn (II)
847   oxidation in a manganese deposit influenced by metal-rich groundwater. *Applied and
848   environmental microbiology* **82**, 3009–3021.

849 Bolton G., LaCasse D. and Kuriyel R. (2006) Combined models of membrane fouling:
850   development and application to microfiltration and ultrafiltration of biological fluids.
851   *Journal of Membrane Science* **277**, 75–84.

852 Bonneville S., Morgan D. J., Schmalenberger A., Bray A., Brown A., Banwart S. A. and
853   Benning L. G. (2011) Tree-mycorrhiza symbiosis accelerate mineral weathering:
854   Evidences from nanometer-scale elemental fluxes at the hypha–mineral interface.
855   *Geochimica et Cosmochimica Acta* **75**, 6988–7005.

856 Braun A., Huggins F. E., Shah N., Chen Y., Wirick S., Mun S. B., Jacobsen C. and Huffman
857   G. P. (2005) Advantages of soft X-ray absorption over TEM-EELS for solid carbon
858   studies—a comparative study on diesel soot with EELS and NEXAFS. *Carbon* **43**,
859   117–124.

860 Bray A. W., Oelkers E. H., Bonneville S., Wolff-Boenisch D., Potts N. J., Fones G. and
861   Benning L. G. (2015) The effect of pH, grain size, and organic ligands on biotite
862   weathering rates. *Geochimica et Cosmochimica Acta* **164**, 127–145.

863 de la Calle Vian C. (1977) Structure des vermiculites: facteurs conditionnant les mouvements
864   des feuillets. PhD thesis, Université Pierre et Marie Curie - CNRS.

865 Calvaruso C., Turpault M.-P. and Frey-Klett P. (2006) Root-Associated Bacteria Contribute to
866   Mineral Weathering and to Mineral Nutrition in Trees: a Budgeting Analysis. *Applied
867   and Environmental Microbiology* **72**, 1258–1266.

868 Camino-Serrano M., Guenet B., Luyssaert S., Ciais P., Bastrikov V., De Vos B., Gielen B.,
869   Gleixner G., Jornet-Puig A., Kaiser K., Kothawala D., Lauerwald R., Peñuelas J.,
870   Schrumpf M., Vicca S., Vuichard N., Walmsley D. and Janssens I. A. (2018)
871   ORCHIDEE-SOM: modeling soil organic carbon (SOC) and dissolved organic carbon
872   (DOC) dynamics along vertical soil profiles in Europe. *Geosci. Model Dev.* **11**, 937–
873   957.

874 Chenu C., Garnier P., Monga O., Moyano F., Pot V., Nunan N., Coucheney E. and Otten W.
875   (2014) Predicting the response of soil organic matter microbial decomposition to
876   moisture. *EGUGA*, 14981.

877 Chorover J. and Amistadi M. K. (2001) Reaction of forest floor organic matter at goethite,
878   birnessite and smectite surfaces. *Geochimica et Cosmochimica Acta* **65**, 95–109.

879 Chukhrov F. and Gorshkov A. (1981) Iron and manganese oxide minerals in soils. *Earth and*
880   *Environmental Science Transactions of The Royal Society of Edinburgh* **72**, 195–200.

881 Cismasu A. C., Michel F. M., Tcaciuc A. P., Tyliszczak T. and Brown Jr G. E. (2011)
882   Composition and structural aspects of naturally occurring ferrihydrite. *Comptes*
883   *Rendus Geoscience* **343**, 210–218.

884 Clemmensen K., Bahr A., Ovaskainen O., Dahlberg A., Ekblad A., Wallander H., Stenlid J.,
885   Finlay R., Wardle D. and Lindahl B. (2013) Roots and associated fungi drive long-
886   term carbon sequestration in boreal forest. *Science* **339**, 1615–1618.

887 Collignon C., Ranger J. and Turpault M. P. (2012) Seasonal dynamics of Al- and Fe-bearing
888   secondary minerals in an acid forest soil: influence of Norway spruce roots (*Picea*
889   *abies* (L.) Karst.). *European Journal of Soil Science* **63**, 592–602.

890 Cotrufo M. F., Soong J. L., Horton A. J., Campbell E. E., Haddix M. L., Wall D. H. and Parton
891   W. J. (2015) Formation of soil organic matter via biochemical and physical pathways
892   of litter mass loss. *Nature Geoscience* **8**, 776–779.

893 Courty P.-E., Buée M., Diedhiou A. G., Frey-Klett P., Le Tacon F., Rineau F., Turpault M.-P.,
894   Uroz S. and Garbaye J. (2010) The role of ectomycorrhizal communities in forest
895   ecosystem processes: New perspectives and emerging concepts. *Soil Biology and*
896   *Biochemistry* **42**, 679–698.

897 Dauer J. M. and Perakis S. S. (2014) Calcium oxalate contribution to calcium cycling in
898   forests of contrasting nutrient status. *Forest Ecology and Management* **334**, 64–73.

899 Dignac M.-F., Derrien D., Barré P., Barot S., Cécillon L., Chenu C., Chevallier T., Freschet G.
900   T., Garnier P., Guenet B., Hedde M., Klumpp K., Lashermes G., Maron P.-A., Nunan
901   N., Roumet C. and Basile-Doelsch I. (2017) Increasing soil carbon storage:
902   mechanisms, effects of agricultural practices and proxies. A review. *Agron. Sustain.*
903   *Dev.* **37**, 14.

904 Dincher M., Calvaruso C. and Turpault M.-P. (2020) Major element residence times in humus
905   from a beech forest: The role of element forms and recycling. *Soil Biology and*
906   *Biochemistry* **141**, 107674.

907 Dixon J. B. and Weed S. B. (1989) *Minerals in soil environments.*, Soil Science Society of
908   America Inc.(SSSA).

909 Dixon J. and Jackson M. (1959) Dissolution of interlayers from intergradient soil clays after
910   preheating at 400 C. *Science* **129**, 1616–1617.

911 Doetterl S., Berhe A. A., Arnold C., Bodé S., Fiener P., Finke P., Fuchslueger L., Griepentrog
912   M., Harden J. W., Nadeu E., Schnecker J., Six J., Trumbore S., Van Oost K., Vogel C.
913   and Boeckx P. (2018) Links among warming, carbon and microbial dynamics
914   mediated by soil mineral weathering. *Nature Geosci* **11**, 589–593.

915 Estes E. R., Andeer P. F., Nordlund D., Wankel S. D. and Hansel C. M. (2017) Biogenic
916   manganese oxides as reservoirs of organic carbon and proteins in terrestrial and
917   marine environments. *Geobiology* **15**, 158–172.

918 Eusterhues K., Neidhardt J., Hädrich A., Küsel K. and Totsche K. U. (2014) Biodegradation
919   of ferrihydrite-associated organic matter. *Biogeochemistry* **119**, 45–50.

920 Eusterhues K., Rennert T., Knicker H., Kögel-Knabner I., Totsche K. U. and Schwertmann U.
921   (2011) Fractionation of Organic Matter Due to Reaction with Ferrihydrite:
922   Coprecipitation versus Adsorption. *Environmental Science & Technology* **45**, 527–
923   533.

924 Eusterhues K., Rumpel C., Kleber M. and Kögel-Knabner I. (2003) Stabilisation of soil
925   organic matter by interactions with minerals as revealed by mineral dissolution and
926   oxidative degradation. *Organic Geochemistry* **34**, 1591–1600.

927 Eusterhues K., Wagner F. E., Häusler W., Hanzlik M., Knicker H., Totsche K. U., Kögel-
928   Knabner I. and Schwertmann U. (2008) Characterization of Ferrihydrite-Soil Organic
929   Matter Coprecipitates by X-ray Diffraction and Mössbauer Spectroscopy. *Environ. Sci.*
930   *Technol.* **42**, 7891–7897.

931 Ezzaïm A., Turpault M.-P. and Ranger J. (1999a) Quantification of weathering processes in
932   an acid brown soil developed from tuff, Beaujolais, France: Part I. Formation of
933   weathered rind. *Geoderma* **87**, 137–154.

934 Ezzaïm A., Turpault M.-P. and Ranger J. (1999b) Quantification of weathering processes in
935   an acid brown soil developed from tuff, Beaujolais, France: Part II. Soil formation.
936   *Geoderma* **87**, 155–177.

937 Finlay R. D., Mahmood S., Rosenstock N., Bolou-Bi E. B., Köhler S. J., Fahad Z., Rosling A.,
938   Wallander H., Belyazid S., Bishop K. and Lian B. (2020) Reviews and syntheses:
939   Biological weathering and its consequences at different spatial levels – from
940   nanoscale to global scale. *Biogeosciences* **17**, 1507–1533.

941 Georgiadis A., Dietel J., Dohrmann R. and Rennert T. (2020) Review Article. What are the
942   nature and formation conditions of hydroxy-interlayered minerals (HIMs) in soil? *J.*
943   *Plant Nutr. Soil Sci.* **183**, 12–26.

944 Gillot F., Righi D. and Elsass F. (2000) Pedogenic Smectites in Podzols from Central Finland:
945   An Analytical Electron Microscopy Study. *Clays and Clay Minerals* **48**, 655–664.

946 Grand S. and Lavkulich L. M. (2013) Potential influence of poorly crystalline minerals on soil
947   chemistry in Podzols of southwestern Canada: Acidic forest soil chemistry. *Eur J Soil*
948   *Sci* **64**, 651–660.

949 Heitmann A. P., Silva G. C., Paiva P. R. P., Dantas M. S. S., Ciminelli V. S., Souza Dinola I.
950   C. and Ferreira A. M. (2016) Magnetized manganese oxide nanocomposite for
951   effective decontamination of Cd (II) from wastewaters. *Water Science and*
952   *Technology* **74**, 2762–2772.

953 Hemingway J. D., Rothman D. H., Grant K. E., Rosengard S. Z., Eglinton T. I., Derry L. A.
954   and Galy V. V. (2019) Mineral protection regulates long-term global preservation of
955   natural organic carbon. *Nature* **570**, 228–231.

956 Hinsinger P., Jaillard B. and Dufey J. E. (1992) Rapid weathering of a trioctahedral mica by
957   the roots of ryegrass. *Soil Science Society of America Journal* **56**, 977–982.

958 Hofrichter M. (2002) lignin conversion by manganese peroxidase (MnP). *Enzyme and*
959   *Microbial technology* **30**, 454–466.

960 Hu C., Deng Y., Hu H., Duan Y. and Zhai K. (2016) Adsorption and intercalation of low and
961   medium molar mass chitosans on/in the sodium montmorillonite. *International Journal*
962   *of Biological Macromolecules* **92**, 1191–1196.

963 Ivarson K. and Heringa P. (1972) Oxidation of manganese by microorganisms in manganese
964   deposits of Newfoundland soil. *Canadian Journal of Soil Science* **52**, 401–416.

965 Jeong G. Y. (1998) Vermicular kaolinite epitactic on primary phyllosilicates in the weathering
966   profiles of anorthosite. *Clays and Clay Minerals* **46**, 12.

967 Johnson K., Purvis G., Lopez-Capel E., Peacock C., Gray N., Wagner T., März C., Bowen L.,
968   Ojeda J., Finlay N., Robertson S., Worrall F. and Greenwell C. (2015) Towards a
969   mechanistic understanding of carbon stabilization in manganese oxides. *Nat*
970   *Commun* **6**, 7628.

971 Kalinowski B. E. and Schweda P. (2007) Rates and nonstoichiometry of vermiculite
972   dissolution at 22°C. *Geoderma* **142**, 197–209.

973 Keil R. G. and Mayer L. M. (2014) Mineral Matrices and Organic Matter. In *Treatise on*
974   *Geochemistry* Elsevier. pp. 337–359.

975 Keiluweit M., Bougoure J. J., Nico P. S., Pett-Ridge J., Weber P. K. and Kleber M. (2015)
976   Mineral protection of soil carbon counteracted by root exudates. *Nature Clim Change*
977   **5**, 588–595.

978 Keiluweit M. and Kleber M. (2009) Molecular-Level Interactions in Soils and Sediments: The
979   Role of Aromatic π-Systems. *Environ. Sci. Technol.* **43**, 3421–3429.

980 Keiluweit M., Wanzek T., Kleber M., Nico P. and Fendorf S. (2017) Anaerobic microsites
981   have an unaccounted role in soil carbon stabilization. *Nature communications* **8**, 1–
982   10.

983 Kiersnowski A., Serwadczak M., Kułaga E., Futoma-Kołoch B., Bugla-Płoskońska G.,
984   Kwiatkowski R., Doroszkiewicz W. and Pigłowski J. (2009) Delamination of
985   montmorillonite in serum—A new approach to obtaining clay-based biofunctional
986   hybrid materials. *Applied Clay Science*, 5.

987 Kleber M., Bourg I. C., Coward E. K., Hansel C. M., Myneni S. C. and Nunan N. (2021)
988   Dynamic interactions at the mineral–organic matter interface. *Nature Reviews Earth &*
989   *Environment* **2**, 402–421.

990 Kleber M., Eusterhues K., Keiluweit M., Mikutta C., Mikutta R. and Nico P. S. (2015) Mineral–
991   Organic Associations: Formation, Properties, and Relevance in Soil Environments. In
992   *Advances in Agronomy* Elsevier. pp. 1–140.

993 Krieger C., Calvaruso C., Morlot C., Uroz S., Salsi L. and Turpault M.-P. (2017) Identification,
994   distribution, and quantification of biominerals in a deciduous forest. *Geobiology* **15**,
995   296–310.

996 Kung K.-H. and McBride M. (1988) Electron transfer processes between hydroquinone and
997   hausmannite (Mn 3 O 4). *Clays and Clay Minerals* **36**, 297–302.

998 Lanson B., Ferrage E., Hubert F., Prêt D., Mareschal L., Turpault M.-P. and Ranger J. (2015)
999   Experimental aluminization of vermiculite interlayers: An X-ray diffraction perspective
1000   on crystal chemistry and structural mechanisms. *Geoderma* **249–250**, 28–39.

Lavallee J. M., Conant R. T., Paul E. A. and Cotrufo M. F. (2018) Incorporation of shoot versus root-derived 13C and 15N into mineral-associated organic matter fractions: results of a soil slurry incubation with dual-labelled plant material. *Biogeochemistry* **137**, 379–393.

Lehmann J. and Kleber M. (2015) The contentious nature of soil organic matter. *Nature* **528**, 60–68.

Leinweber P. and Schulten H.-R. (1995) Composition, stability and turnover of soil organic matter: investigations by off-line pyrolysis and direct pyrolysis-mass spectrometry. *Journal of Analytical and Applied Pyrolysis* **32**, 91–110.

Li H., Santos F., Butler K. and Herndon E. (2021a) A Critical Review on the Multiple Roles of Manganese in Stabilizing and Destabilizing Soil Organic Matter. *Environmental Science & Technology*.

Li, H., Bölscher, T., Winnick, M., Tfaily, M. M., Cardon, Z. G., & Keiluweit, M. (2021b). Simple Plant and Microbial Exudates Destabilize Mineral-Associated Organic Matter via Multiple Pathways. Environmental Science & Technology, **55**(5), 3389-3398.

Li S., He H., Tao Q., Zhu J., Tan W., Ji S., Yang Y. and Zhang C. (2020) Kaolinization of 2:1 type clay minerals with different swelling properties. *American Mineralogist* **105**, 687–696.

Likens G. E. (2013) *Biogeochemistry of a forested ecosystem.*, Springer Science & Business Media.

Luo Y., Tan W., Suib S. L., Qiu G. and Liu F. (2018) Dissolution and phase transformation processes of hausmannite in acidic aqueous systems under anoxic conditions. *Chemical Geology* **487**, 54–62.

Lutfalla S., Barré P., Bernard S., Le Guillou C., Alléon J. and Chenu C. (2019) Multidecadal persistence of organic matter in soils: multiscale investigations down to the submicron scale. *Biogeosciences* **16**, 1401–1410.

Mareschal L., Ranger J. and Turpault M. P. (2009) Stoichiometry of a dissolution reaction of a trioctahedral vermiculite at pH 2.7. *Geochimica et Cosmochimica Acta* **73**, 307–319.

Mareschal L., Turpault M.-P., Bonnaud P. and Ranger J. (2013) Relationship between the weathering of clay minerals and the nitrification rate: a rapid tree species effect. *Biogeochemistry* **112**, 293–309.

Marques R. (1996) Dynamique du fonctionnement minéral d'une plantation de Douglas (Pseudotsuga menziesii (Mirb.) Franco) dans les Monts du Beaujolais (France). PhD thesis, Ecole nationale du génie rural, des eaux et des forêts.

Marques R. and Ranger J. (1997) Nutrient dynamics in a chronosequence of Douglas-fir !Pseudotsuga menziesii (Mirb.) France) stands on the Beaujolais Mounts (France). 1: Qualitative approach. **91**, 255–277.

Mathieu J. A., Hatté C., Balesdent J. and Parent É. (2015) Deep soil carbon dynamics are driven more by soil type than by climate: a worldwide meta-analysis of radiocarbon profiles. *Glob Change Biol* **21**, 4278–4292.

Mayanna S., Peacock C. L., Schäffner F., Grawunder A., Merten D., Kothe E. and Büchel G. (2015) Biogenic precipitation of manganese oxides and enrichment of heavy metals at acidic soil pH. *Chemical Geology* **402**, 6–17.

McKenzie R. (1972) The sorption of some heavy metals by the lower oxides of manganese. *Geoderma* **8**, 29–35.

Mehra O. and Jackson M. (1960) Iron oxide removal from soils and clays by a dithionite–citrate system buffered with sodium bicarbonate. In *Clays and clay minerals* Elsevier. pp. 317–327.

Meunier A. (2007) Soil hydroxy-interlayered minerals: a re-interpretation of their crystallochemical properties. *Clays and Clay Minerals* **55**, 9.

Mikutta C. (2011) X-ray absorption spectroscopy study on the effect of hydroxybenzoic acids on the formation and structure of ferrihydrite. *Geochimica et Cosmochimica Acta* **75**, 5122–5139.

Mikutta C. and Kretzschmar R. (2008) Synthetic coprecipitates of exopolysaccharides and ferrihydrite. Part II: Siderophore-promoted dissolution. *Geochimica et Cosmochimica Acta* **72**, 1128–1142.

Mikutta R., Kleber M. and Jahn R. (2005) Poorly crystalline minerals protect organic carbon in clay subfractions from acid subsoil horizons. *Geoderma* **128**, 106–115.

Mikutta R., Lorenz D., Guggenberger G., Haumaier L. and Freund A. (2014) Properties and reactivity of Fe-organic matter associations formed by coprecipitation versus adsorption: Clues from arsenate batch adsorption. *Geochimica et Cosmochimica Acta* **144**, 258–276.

Mikutta R., Schaumann G. E., Gildemeister D., Bonneville S., Kramer M. G., Chorover J., Chadwick O. A. and Guggenberger G. (2009) Biogeochemistry of mineral–organic associations across a long-term mineralogical soil gradient (0.3–4100kyr), Hawaiian Islands. *Geochimica et Cosmochimica Acta* **73**, 2034–2060.

Mikutta R., Turner S., Schippers A., Gentsch N., Meyer-Stüve S., Condron L. M., Peltzer D. A., Richardson S. J., Eger A., Hempel G., Kaiser K., Klotzbücher T. and Guggenberger G. (2019) Microbial and abiotic controls on mineral-associated organic matter in soil profiles along an ecosystem gradient. *Sci Rep* **9**, 10294.

Miltner A., Bombach P., Schmidt-Brücken B. and Kästner M. (2012) SOM genesis: microbial biomass as a significant source. *Biogeochemistry* **111**, 41–55.

Monvisade P. and Siriphannon P. (2009) Chitosan intercalated montmorillonite: Preparation, characterization and cationic dye adsorption. *Applied Clay Science* **42**, 427–431.

Mouvenchery K. Y., Kučerík J., Diehl D. and Schaumann G. E. (2012) Cation-mediated cross-linking in natural organic matter: a review. *Rev Environ Sci Biotechnol* **11**, 41–54.

MurakamLii T., Kasama T. and Sato M. (2002) Biotitization of vermiculite under hydrothermal condition. *Journal of mineralogical and petrological sciences* **97**, 263–268.

Nagy K. L. (1995) Chapter 5. Dissolution and precipitation kinetics of sheet silicates. In *Chemical Weathering Rates of Silicate Minerals* (eds. A. F. White and S. L. Brantley). De Gruyter, Berlin, Boston. pp. 173–234.

Newcomb C. J., Qafoku N. P., Grate J. W., Bailey V. L. and De Yoreo J. J. (2017) Developing a molecular picture of soil organic matter–mineral interactions by quantifying organo–mineral binding. *Nat Commun* **8**, 396.

Nielsen L. E. (1967) Models for the permeability of filled polymer systems. *Journal of Macromolecular Science—Chemistry* **1**, 929–942.

Pinzari F., Cuadros J., Migliore M., Napoli R. and Najorka J. (2018) Manganese translocation and concentration on Quercus cerris decomposing leaf and wood litter by an ascomycetous fungus: an active process with ecosystem consequences? *FEMS microbiology ecology* **94**, fiy111.

Pinzari F., Cuadros J., Napoli R., Canfora L. and Baussà Bardají D. (2016) Routes of phlogopite weathering by three fungal strains. *Fungal Biology* **120**, 1582–1599.

Qian A., Zhang W., Shi C., Pan C., Giammar D. E., Yuan S., Zhang H. and Wang Z. (2019) Geochemical stability of dissolved Mn (III) in the presence of pyrophosphate as a model ligand: Complexation and disproportionation. *Environmental science & technology* **53**, 5768–5777.

Ranger J., Dambrine E., Robert M., Righi D. and Felix C. (1991) Study of current soil-forming processes using bags of vermiculite and resins placed within soil horizons. *Geoderma* **48**, 335–350.

Ranger J., Marques R. and Colin-Belgrand M. (1997) Nutrient dynamics during the development of a Douglas-fir (Pseudotsuga menziesii Mirb.) stand. *Acta Oecologica* **18**, 73–90.

Ranger J., Marques R., Colin-Belgrand M., Flammang N. and Gelhaye D. (1995) The dynamics of biomass and nutrient accumulation in a Douglas-fir (Pseudotsuga menziesii Franco) stand studied using a chronosequence approach. *Forest Ecology and Management* **72**, 167–183.

Ranger J. and Turpault M.-P. (1999) Input–output nutrient budgets as a diagnostic tool for sustainable forest management. *Forest ecology and management* **122**, 139–154.

Rasmussen C., Heckman K., Wieder W. R., Keiluweit M., Lawrence C. R., Berhe A. A., Blankinship J. C., Crow S. E., Druhan J. L., Hicks Pries C. E., Marin-Spiotta E., Plante A. F., Schädel C., Schimel J. P., Sierra C. A., Thompson A. and Wagai R. (2018) Beyond clay: towards an improved set of variables for predicting soil organic matter content. *Biogeochemistry* **137**, 297–306.

Reardon P. N., Walter E. D., Marean-Reardon C. L., Lawrence C. W., Kleber M. and Washton N. M. (2018) Carbohydrates protect protein against abiotic fragmentation by soil minerals. *Scientific reports* **8**, 1–8.

Remusat L., Hatton P.-J., Nico P. S., Zeller B., Kleber M. and Derrien D. (2012) NanoSIMS Study of Organic Matter Associated with Soil Aggregates: Advantages, Limitations, and Combination with STXM. *Environ. Sci. Technol.* **46**, 3943–3949.

Rich C. (1968) Hydroxy interlayers in expansible layer silicates. *Clays and Clay Minerals* **16**, 15–30.

Rogelj J., Shindell D., Jiang K., Fifita S., Forster P., Ginzburg V., Handa C., Kobayashi S., Kriegler E., Mundaca L., Séférian R., Vilariño M. V., Calvin K., Emmerling J., Fuss S., Gillett N., He C., Hertwich E., Höglund-Isaksson L., Huppmann D., Luderer G.,

McCollum D. L., Meinshausen M., Millar R., Popp A., Purohit P., Riahi K., Ribes A., Saunders H., Schädel C., Smith P., Trutnevyte E., Xiu Y., Zhou W., Zickfeld K., Flato G., Fuglestvedt J., Mrabet R. and Schaeffer R. (2018) Mitigation Pathways Compatible with 1.5°C in the Context of Sustainable Development. , 82.

Romero R., Robert M., Elsass F. and Garcia C. (1992) Evidence by transmission electron microscopy of weathering microsystems in soils developed from crystalline rocks. *Clay miner.* **27**, 21–33.

Rouiller J., Guillet B. and Bruckert S. (1980) Cations acides échangeables et acidités de surface: Approche analytique et incidences pédogénétiques. *Sciences du Sol - AFES* **2**, 161–175.

Rowley M. C., Grand S. and Verrecchia É. P. (2018) Calcium-mediated stabilisation of soil organic carbon. *Biogeochemistry* **137**, 27–49.

Schmidt M. W. I., Torn M. S., Abiven S., Dittmar T., Guggenberger G., Janssens I. A., Kleber M., Kögel-Knabner I., Lehmann J., Manning D. A. C., Nannipieri P., Rasse D. P., Weiner S. and Trumbore S. E. (2011) Persistence of soil organic matter as an ecosystem property. *Nature* **478**, 49–56.

Skiba M., Szczerba M., Skiba S., Bish D. L. and Grybos M. (2011) The nature of interlayering in clays from a podzol (Spodosol) from the Tatra Mountains, Poland. *Geoderma* **160**, 425–433.

Smits M. and Wallander H. (2017) Role of mycorrhizal symbiosis in mineral weathering and nutrient mining from soil parent material. In *Mycorrhizal mediation of soil* Elsevier. pp. 35–46.

Solomon D., Lehmann J., Wang J., Kinyangi J., Heymann K., Lu Y., Wirick S. and Jacobsen C. (2012) Micro-and nano-environments of C sequestration in soil: A multi-elemental STXM–NEXAFS assessment of black C and organomineral associations. *Science of the total environment* **438**, 372–388.

Sowers T. D., Stuckey J. W. and Sparks D. L. (2018) The synergistic effect of calcium on organic carbon sequestration to ferrihydrite. *Geochem Trans* **19**, 4.

Sposito G. (2008) *The chemistry of soils.*, Oxford university press.

Stockmann U., Adams M. A., Crawford J. W., Field D. J., Henakaarchchi N., Jenkins M., Minasny B., McBratney A. B., Courcelles V. de R. de, Singh K., Wheeler I., Abbott L., Angers D. A., Baldock J., Bird M., Brookes P. C., Chenu C., Jastrow J. D., Lal R., Lehmann J., O'Donnell A. G., Parton W. J., Whitehead D. and Zimmermann M. (2013) The knowns, known unknowns and unknowns of sequestration of soil organic carbon. *Agriculture, Ecosystems & Environment* **164**, 80–99.

Stumm W. and Morgan J. J. (1996) Aquatic chemistry: chemical equilibria and rates in natural waters, paperback.

Taghaddosi S., Akbari A. and Yegani R. (2017) Preparation, characterization and anti-fouling properties of nanoclays embedded polypropylene mixed matrix membranes. *Chemical Engineering Research and Design* **125**, 35–45.

Tamm O. (1922) Eine Methode zur Bestim mung der anorganischen Komponenten des Gelkomplexes im Boden. *Meddel. Statens Skogsforsoksanst.* **19**, 385–404.

1169 Tamrat W. Z., Rose J., Grauby O., Doelsch E., Levard C., Chaurand P. and Basile-Doelsch I.
1170   (2018) Composition and molecular scale structure of nanophases formed by
1171   precipitation of biotite weathering products. *Geochimica et Cosmochimica Acta* **229**,
1172   53–64.

1173 Tamrat W. Z., Rose J., Grauby O., Doelsch E., Levard C., Chaurand P. and Basile-Doelsch I.
1174   (2019) Soil organo-mineral associations formed by co-precipitation of Fe, Si and Al in
1175   presence of organic ligands. *Geochimica et Cosmochimica Acta* **260**, 15–28.

1176 Tan P., Oberhardt N., Dypvik H., Riber L. and Ferrell R. E. (2017) Weathering profiles and
1177   clay mineralogical developments, Bornholm, Denmark. *Marine and Petroleum*
1178   *Geology* **80**, 32–48.

1179 Tang Y., Zeiner C. A., Santelli C. M. and Hansel C. M. (2013) Fungal oxidative dissolution of
1180   the Mn(II)-bearing mineral rhodochrosite and the role of metabolites in manganese
1181   oxide formation: Dissolution and oxidation of rhodochrosite by fungi. *Environ Microbiol*
1182   **15**, 1063–1077.

1183 Turpault M.-P., Calvaruso C., Dincher M., Mohammed G., Didier S., Redon P.-O. and Cochet
1184   C. (2019) Contribution of carbonates and oxalates to the calcium cycle in three beech
1185   temperate forest ecosystems with contrasting soil calcium availability.
1186   *Biogeochemistry* **146**, 51–70.

1187 Turpault M.-P., Gobran G. R. and Bonnaud P. (2007) Temporal variations of rhizosphere and
1188   bulk soil chemistry in a Douglas fir stand. *Geoderma* **137**, 490–496.

1189 Turpault M.-P., Nys C. and Calvaruso C. (2009) Rhizosphere impact on the dissolution of test
1190   minerals in a forest ecosystem. *Geoderma* **153**, 147–154.

1191 Turpault M.-P. and Trotignon L. (1994) The dissolution of biotite single crystals in dilute
1192   HNO3 at 24 C: Evidence of an anisotropic corrosion process of micas in acidic
1193   solutions. *Geochimica et Cosmochimica Acta* **58**, 2761–2775.

1194 Vermeire M.-L. (2017) Evolution of carbon stabilization mechanisms in a podzolic soil
1195   chronosequence.

1196 Vogel C., Mueller C. W., Höschen C., Buegger F., Heister K., Schulz S., Schloter M. and
1197   Kögel-Knabner I. (2014) Submicron structures provide preferential spots for carbon
1198   and nitrogen sequestration in soils. *Nat Commun* **5**, 2947.

1199 Wallander H. and Wickman T. (1999) Biotite and microcline as potassium sources in
1200   ectomycorrhizal and non-mycorrhizal Pinus sylvestris seedlings. *Mycorrhiza* **9**, 25–32.

1201 Wang J., Li J., Jiang C., Zhou P., Zhang P. and Yu J. (2017) The effect of manganese
1202   vacancy in birnessite-type MnO 2 on room-temperature oxidation of formaldehyde in
1203   air. *Applied Catalysis B: Environmental* **204**, 147–155.

1204 Wilson M. (1966) The weathering of biotite in some Aberdeenshire soils. *Mineralogical*
1205   *Magazine and Journal of the Mineralogical Society* **36**, 1080–1093.

1206 Zhou H. and Fu C. (2020) Manganese-oxidizing microbes and biogenic manganese oxides:
1207   characterization, Mn (II) oxidation mechanism and environmental relevance. *Reviews*
1208   *in Environmental Science and Bio/Technology*, 1–19.

1209

7 Tables

Table 1 – Forest floor and soil horizons properties of the experimental site. Al_{AO}: Al extracted by ammonium oxalate (Tamm, 1922); Fe_{DBC}: Fe extracted by dithionite-citrate-bicarbonate (Mehra and Jackson, 1960). pH_w: pH measured in water. CEC: cation exchange capacity. BC/CEC: base saturation. Data from Ranger et al. (1995, 1997), Marques and Ranger (1997) and Ezzaïm et al. (1999a).

Horizon	Depth (cm)	pH_w	Granulometry (%)			Total elements (mg g^{-1})					Free elements (mg g^{-1})		Exchangeable cations (cmol$_c$ kg^{-1})								CEC (cmol$_c$ kg^{-1})	BC/CEC (%)
			clay	Silt	sand	C	C/N	Ca	Mg	K	Al_{AO}	Fe_{DCB}	K	Ca	Mg	Mn	Fe	Na	H	Al		
OL		3.8				393	36	6.8	0.5	1.3												
OF+OH						251	23	3.1	2.9	8.8												
A1/Ap	0-10	4.3	20	41	40	47	13	0.9	5.0	31.7	6.2	9.3	0.20	0.18	0.15	0.07	0.02	0.05	0.54	7.52	8.7	7.7
Ap2	10-20	4.6	20	43	37	22	11	0.8	4.9	33.0	4.6	8.6	0.19	0.08	0.07	0.03	0.00	0.11	0.24	4.37	5.1	9.4
Ap	20-35	4.5	22	42	36	18	12	0.8	5.7	33.8	3.9	9.0	0.15	0.07	0.05	0.03	0.00	0.02	0.19	4.46	5.0	6.4
B1	35-50	4.5	25	40	35	7	10	0.6	6.2	34.8	3.3	9.0	0.13	0.06	0.03	0.02	0.00	0.00	0.16	4.08	4.5	5.4

Table 2 – Exchangeable cations, cation exchange capacity (CEC) and contribution of each exchangeable cation to the CEC, for the control vermiculite (V0) and the 20 year weathered vermiculite (V20) samples (mean and standard deviation of four independent samples for V0 and three for V20). EA/CEC: exchange acidity (sum of H and Al cations). Exact Two-Sample Fisher-Pitman Permutation Test significant differences between V0 and V20: *** p-value < 0.001; ** p-value < 0.01; * p-value < 0.05.

Exchangeable cations and CEC ($cmol_c\ kg^{-1}$)									
Sample	Na	K	Ca	Mg	Mn	Fe	H	Al	CEC
V0	173.6 (1.2)	0.00 (0.00)	0.53 (0.01)	2.83 (0.02)	0.01 (0.00)	0.01 (0.00)	0.67 (0.16)	0.46 (0.03)	178.1 (1.2)
V20	0.00***	0.31 (0.14)**	20.95 (13.25)**	14.11 (8.74)*	4.63 (0.92)***	0.22 (0.12)**	6.09 (3.06)**	2.93 (0.89)***	49.2 (19.1)***

Exchangeable cations percentage in CEC (%)								
Na/CEC	K/CEC	Ca/CEC	Mg/CEC	Mn/CEC	Fe/CEC	H/CEC	Al/CEC	EA/CEC
97.5	0.00	0.3	1.6	0.01	0.01	0.38	0.26	0.60
0.0	0.63	42.6	28.7	9.40	0.44	12.36	5.96	18.3

1221   Table 3 – Total chemical analysis of control vermiculite (V0) and weathered vermiculite (V20) samples (mean and standard deviation of four

1222   independent samples for V0 and for each V20 mineral bags – average of V20 mineral bags analyses is also given). Exact Two-Sample Fisher-

1223   Pitman Permutation Test Significant differences between V0 and V20: *** p-value < 0.001; ** p-value < 0.01; * p-value < 0.05, n.s. non-

1224   significant p-value >0.05.

Sample	Oxides (wt %)										C (wt%)
	SiO_2	Al_2O_3	Fe_2O_3	MnO	MgO	CaO	Na_2O	K_2O	TiO_2	Total oxide	
V0	40.06 (0.62)	17.59 (0.24)	4.95 (0.06)	0.13 (0.002)	24.57 (0.31)	0.41 (0.03)	6.25 (0.06)	0.00	0.31 (0.00)	94.26 (1.27)	0.08 (0.01)
V20 I	35.50 (0.38)***	17.09 (0.27)*	4.48 (0.05)***	0.70 (0.12)**	22.20 (0.23)***	1.05 (0.21)*	0.00***	0.30 (0.01)***	0.30 (0.00) n.s.	81.61 (0.77)***	0.64 (0.01)***
V20 II	35.17 (0.28)***	17.43 (0.1) n.s.	4.45 (0.05)***	0.41 (0.01)***	21.28 (0.22)***	0.47 (0.01)*	0.00***	0.26 (0.00)***	0.31 (0.00) n.s.	79.78 (0.65)***	0.65 (0.00)***
V20 III	35.84 (0.34)***	17.90 (0.14) n.s.	4.54 (0.05)***	0.45 (0.01)***	21.73 (0.19)***	0.46 (0.00) n.s.	0.00***	0.19 (0.00)***	0.30 (0.00)*	81.41 (0.70)***	0.43 (0.02)***
average V20	35.50 (0.44)***	17.47 (0.38) n.s.	4.49 (0.06)***	0.52 (0.15)***	21.73 (0.43)***	0.66 (0.30)*	0.00***	0.25 (0.05)***	0.30 (0.00) n.s.	80.93 (1.08)***	0.57 (0.10)***

1225

1226 Table 4 – Mineral chemical element composition of weathered vermiculite FIBs and control vermiculite FIB (V0n) using TEM-EDS analysis
1227 expressed in normalized counts, to account for the variations in FIB section thickness. V0n – control vermiculite at the nano-scale (n=34); V20n
1228 – weathered vermiculite at the nano-scale (n=38); ES E – Exfoliation Spaces Empty (n=3); ES Si - Exfoliation Spaces enriched in Si (n=7); ES
1229 Ca – Exfoliation Spaces enriched in Ca (n=21); MnOx – Manganese Oxide (n=38); SiAl – aluminosilicates (n=17); SiAlK – K-rich aluminosilicate
1230 (n=6). Levels of significance of Exact Two-Sample Fisher-Pitman Permutation Test comparing V0 to the various weathered mineral zones in the
1231 FIBs extracted from the V20 particle: * p-value < 0.05, ** p-value < 0.01, *** p-value < 0.001. n.s. non-significant. When no standard deviation is
1232 indicated, the element quantity was under the detection limit and was assumed to be equal to 0 for statistical purposes.

Localization	Mineral Zone	Elemental composition (normalized counts %)									
		C	K	Na	Mg	Al	Si	Ca	Ti	Mn	Fe
Vermiculite Matrix	V0n	4.80 (0.36)	0.10 (0.10)	5.67 (0.62)	30.37 (0.60)	18.32 (0.38)	33.79 (0.76)	0.27 (0.1)	0.33 (0.16)	0.23 (0.22)	6.12 (0.4)
	V20n	4.93 (0.41) n.s.	0.14 (0.10) n.s.	0.00***	29.10 (1.04)***	17.69 (0.43)***	34.53 (0.56)***	4.34 (0.78)***	0.06 (0.14)***	0.74 (0.22)***	8.47 (0.55)***
Nano-scale Exfoliation Spaces	ES E	4.50 (0.16) n.s.	0.00***	0.00***	30.09 (1.18) n.s.	17.87 (0.44) n.s.	35.86 (0.77) n.s.	3.29 (0.24)***	0.00***	0.88 (0.09)***	7.51 (0.15)***
	ES Si	5.41 (0.51) *	0.00***	0.00***	26.60 (1.47)***	16.97 (0.74)***	39.23 (1.21)***	3.47 (0.36)***	0.00***	0.59 (0.18)***	7.77 (0.63)***
	ES Ca	6.11 (0.78)***	0.25 (0.11)***	0.00***	26.32 (1.91)***	16.36 (0.95)***	33.12 (1.17)*	8.58 (2.39)***	0.09 (0.14)***	0.61 (0.19)***	8.57 (0.46)***
Micro-scale Exfoliation Space	MnOx	7.74 (0.93)***	0.00 **	0.00***	0.23 (0.15)***	0.72 (0.31)***	1.47 (0.70)***	5.90 (0.49)***	0.00***	78.78 (1.52)***	5.15 (0.64) n.s.
	SiAl	5.15 (0.68) n.s.	0.6 (0.73)*	0.00***	0.66 (0.39)***	40.89 (3.16)***	45.08 (1.60)***	0.23 (0.18) n.s.	0.22 (0.65) n.s.	1.90 (1.52)***	5.27 (1.77) n.s.
	SiAlK	8.10 (1.77)**	17.79 (1.06)***	0.00***	0.69 (0.30)***	15.72 (2.42) n.s.	43.67 (1.53)***	0.54 (0.30) n.s.	0.00***	7.30 (2.09)***	6.21 (1.64) n.s.

1233

1234

1235

8 Legends of Figures

Figure 1 – XRD patterns of V0 and V20 samples with no treatment and after K-saturation or/and heating treatments (110°C, 330°C and 550°C).

Figure 2 – Scanning Electron Microcopy (SEM) of control vermiculite (V0) outer-surface and of weathered vermiculite (V20) outer- and inner-surfaces. a) SEM-back scattering electron (BSE) images of V0 and b) SEM-secondary electron (SE) images of V0 showing un-weathered smooth surfaces. c) SEM-BSE image of V20 outer-surfaces showing cracks and deposits. d and e) SEM-SE and SEM-BSE details of c. white arrow: possible presence of hyphae. f) detail of e. white arrow: calcium oxalate crystals. g) SEM-BSE image of V20 outer-surfaces showing large Mn-rich and C-rich deposits (Mn dominance in white deposits, C dominance in dark deposits). h) Detail of g). i) EDS spectrum of the white Mn-rich deposits found in h). j) EDS spectrum of the Ca oxalate crystals found in f. k) SEM-BSE image of V20 inner-surfaces showing large Mn-rich or C-rich deposits. l) detail of k. The samples in images a, b, c, d, e and f were coated by graphite. The samples in images g, h, k and l were not coated.

Figure 3 – TEM images of V0n showing the vermiculite matrix on a FIB extracted from a control vermiculite particle. a) High-angle annular dark-field scanning transmission electron microscopy (HAADF-STEM) image. b) electron diffraction pattern showing a crystalline structure, the d001 interplanar spacing of 1 nm is typical of dehydrated vermiculite under TEM vacuum. c to h) EDS maps of Si, Al, Na, Mg, C and Ca, respectively.

Figure 4 - FIB section extracted from the 20-year weathered vermiculite particle (inner part). a) Location of the FIB section (α - β), on the inner-surface of a 20-year weathered vermiculite particle, exposed by cutting the whole particle along large exfoliation space (copy from Figure

1262 2k). b) SEM image of FIB section downwards into the Mn oxide and the mineral matrix of the

1263 weathered vermiculite particle.

1264

1265 Figure 5 – Bright Field-STEM (BF-STEM) image and EDS maps of two regions of interest in

1266 the mineral matrix of the weathered vermiculite particle. White arrows show nano-scale

1267 empty exfoliation spaces (ES E), black arrows show nano-scale exfoliation spaces filled with

1268 C and Si (ES Si), grey arrows show nano-scale exfoliation spaces filled with C and Ca (ES

1269 Ca).

1270

1271 Figure 6 – Mn deposit characterization. a) center: BF-STEM image 340 nm x 340 nm. Dark

1272 zones correspond to Mn enrichment and paler zones correspond to low density matter (e.g.

1273 SOM or pores); left: electron diffraction pattern; right: TEM-EDS mapping of the major

1274 elements of the BF-STEM image and C and Mn TEM-EDS profiles showing the anti-

1275 correlation between Mn and C normalized counts (adjusted R-squared = 0.2, p-value = 8e^{-}

1276 ^{14}).The yellow rectangles correspond to the analyzed area, where darker zones indicate

1277 lower Mn concentration. We acquired 8 other profiles that all showed the same significant

1278 anticorrelation between Mn and C. b) center: BF-STEM image 50 nm x 50 nm; left: electronic

1279 diffraction pattern. The numbers 1 to 4 indicate the d-spacing used to identify the Mn deposit

1280 as hausmannite. c) EELS spectrum collected at the Mn K-edge. Peaks at 642 eV and 653 eV

1281 confirm hausmannite identification.

1282

1283 Figure 7 - BF-STEM image and EDS elemental mapping of the secondary minerals inside a

1284 micro-scale exfoliation space, showing heterogeneous chemical composition. Six zones were

1285 distinguished: V20n – weathered Vermiculite matrix; MnOx – Manganese Oxide deposit; SiAl

1286 – aluminosilicate; SiAlK – K-rich aluminosilicate.

1287

1288 Figure 8 - C content of the different zones identified on the FIB section of the 20 year

1289 weathered vermiculite particle. C content is normalized by the sum of element counts to

1290 account for the variations in FIB section thickness. Comparison with the control vermiculite.

1291 Levels of significance of the Exact Two-Sample Fisher-Pitman Permutation Test are: n.s. -

1292 non-significant, * p-value < 0.05, ** p-value < 0.01, *** p-value < 0.001. Permutational

1293 MANOVA p-value $< 2e^{-16}$.

1294

1295 Figure 9 – TEM-EELS C K-edge spectra of control vermiculite (V0n), of the Ca-and C-rich

1296 material filling the nano-scale exfoliation spaces (ES Ca), and of the Mn oxide (MnOx). The

1297 peak at 287 eV was not very specific and could be assigned to aliphatic, aromatic, or

1298 carbonyl moieties, the peak at 289 eV was assigned to alcohol or carboxyl functional groups,

1299 at 290 eV to carboxylic functional group and at 292 eV to C=C bond resonance (Braun et al.,

1300 2005; Solomon et al., 2012).

1301

1302 Figure 10 – Mass balance weathering during 20 years in topsoil for 100g of initial vermiculite

1303 on an iso-element basis (Ti).

1304

1305 Figure 11 – C content as a function of Ca content in the weathered vermiculite FIB, V20n,

1306 and Exfoliation Spaces filled with Ca, ES Ca. Each symbol represents one measurement

1307 performed over a region of interest. C and Ca are normalized by the sum of EDS element

1308 counts to account for the variations in FIB section thickness.

9 Figures

1310 **Figure 1**
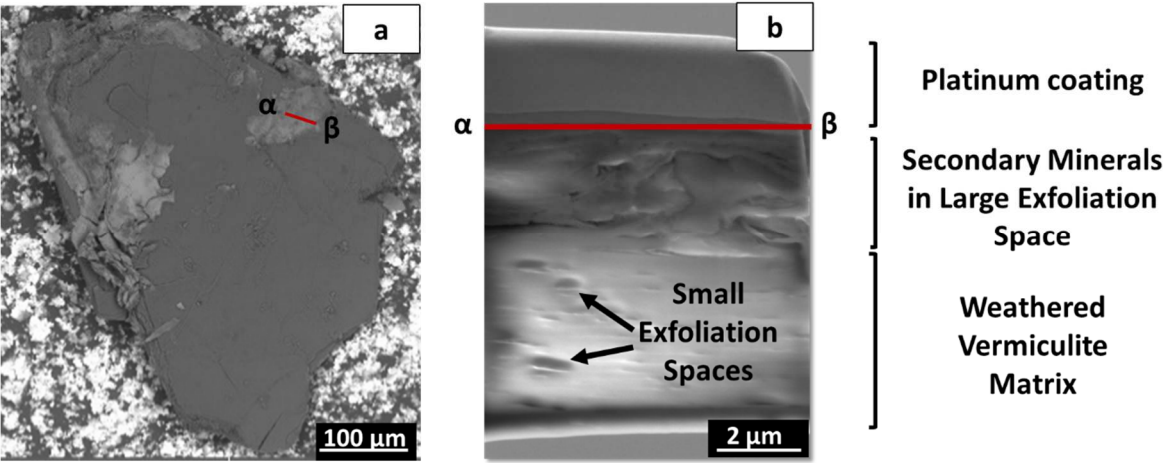

1311

1312

1313 **Figure 2**

51
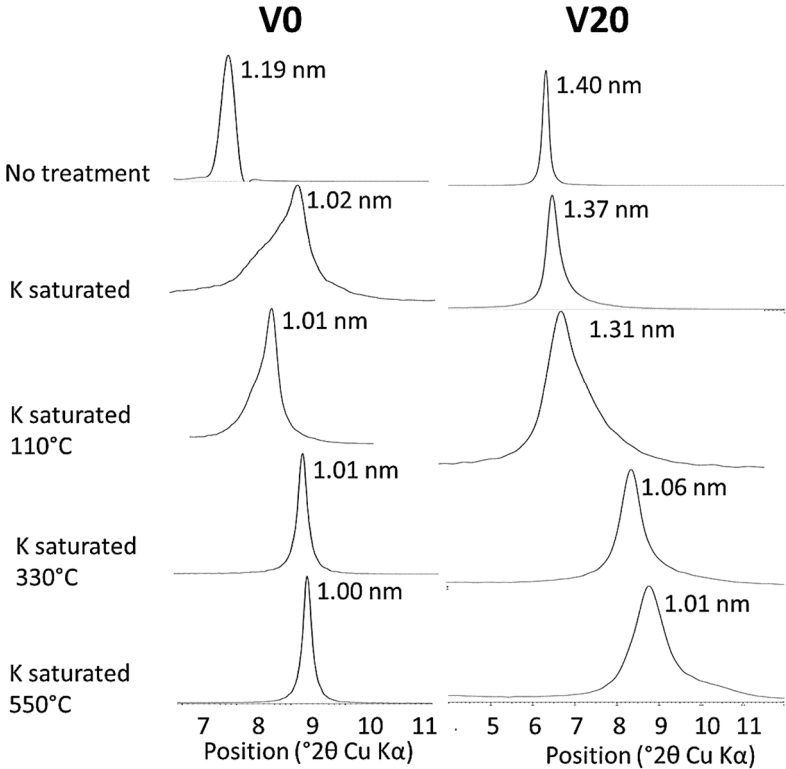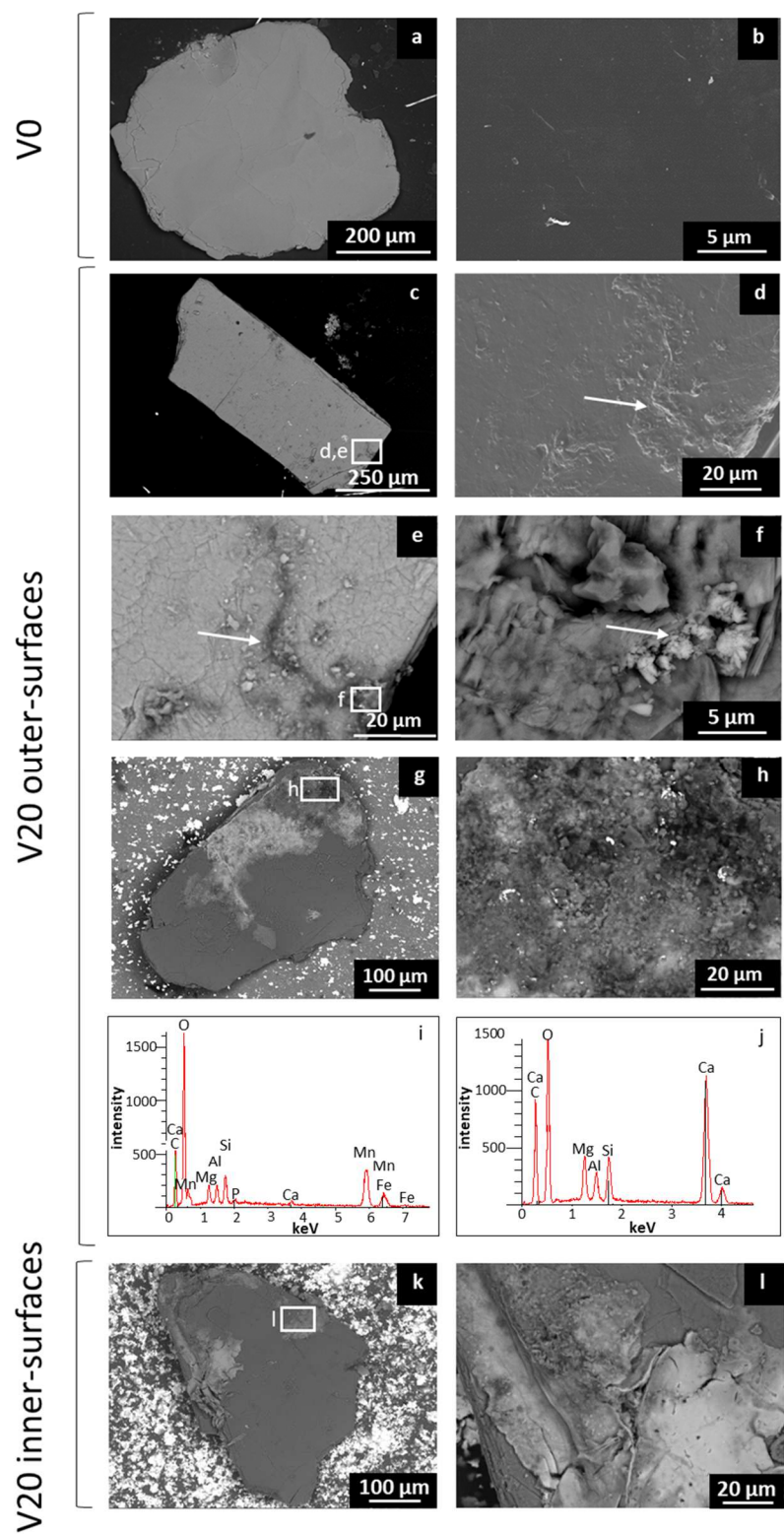
1316 **Figure 3**
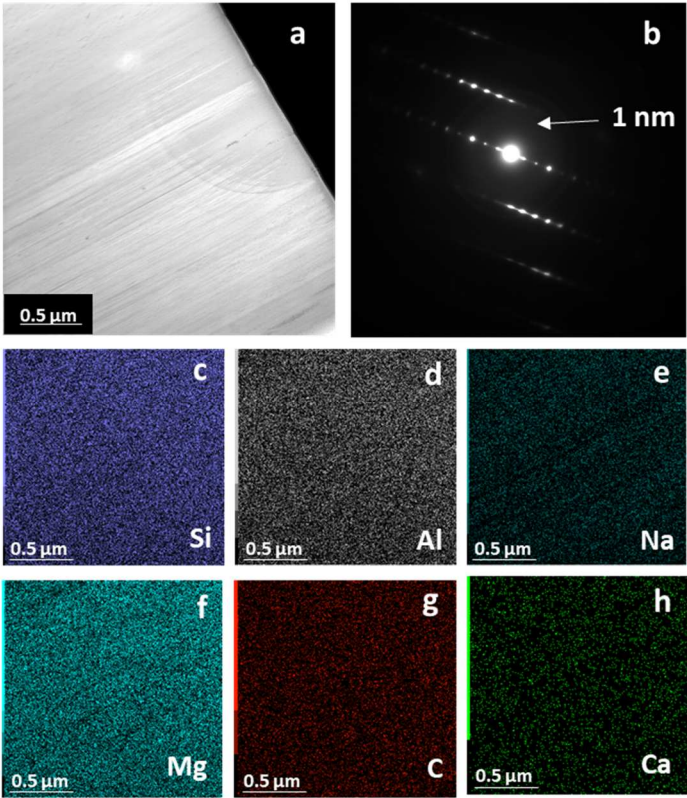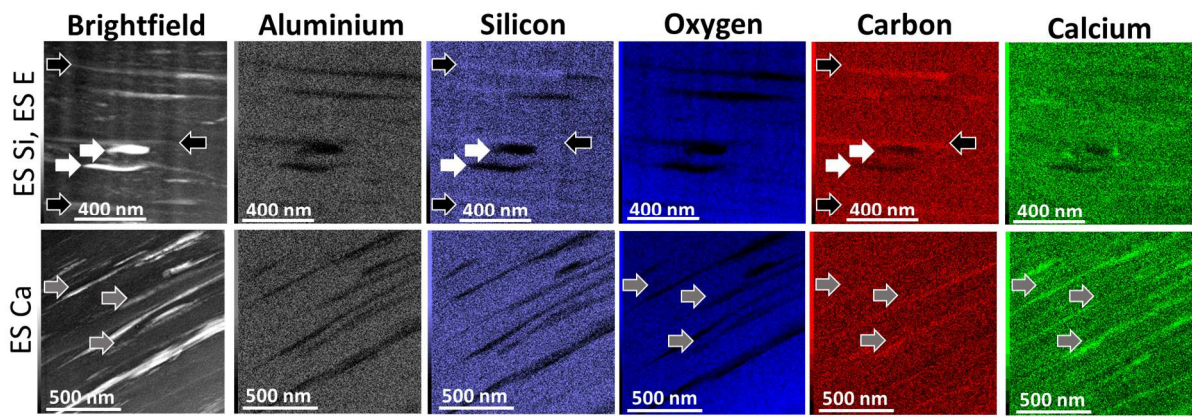

1317

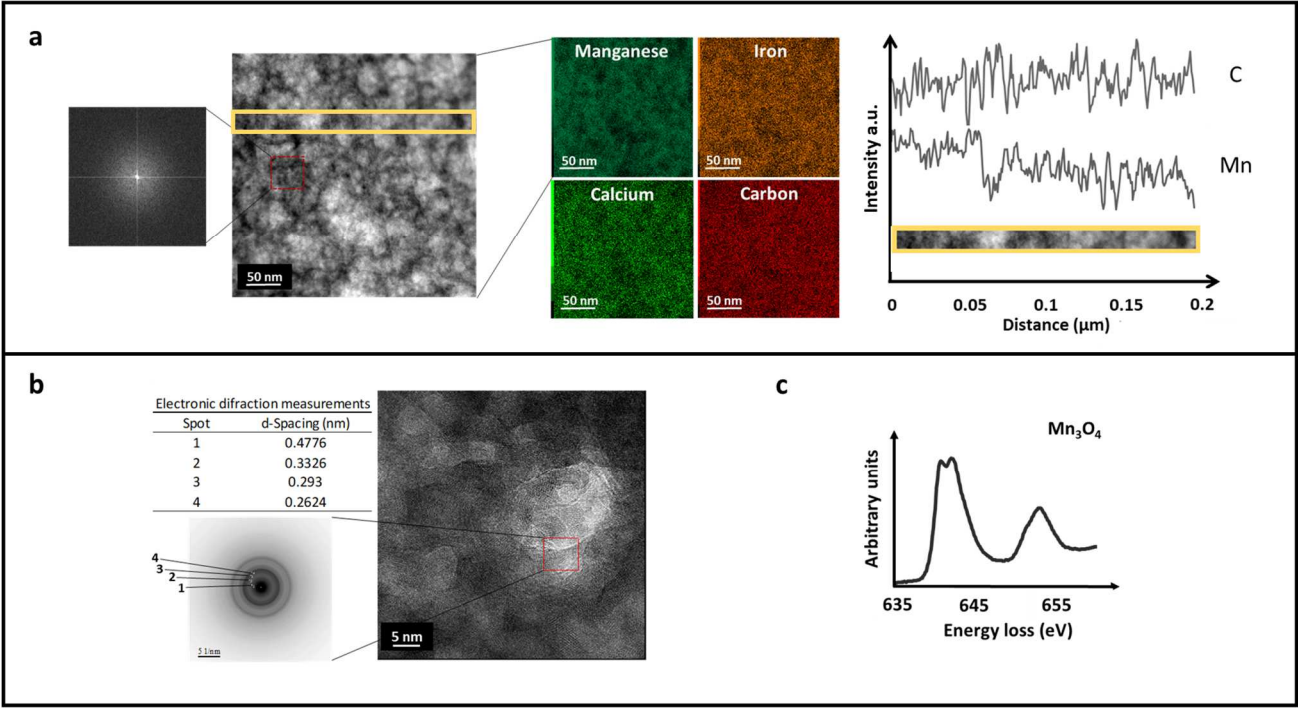1318 **Figure 4**

1319

1320

1321

1322

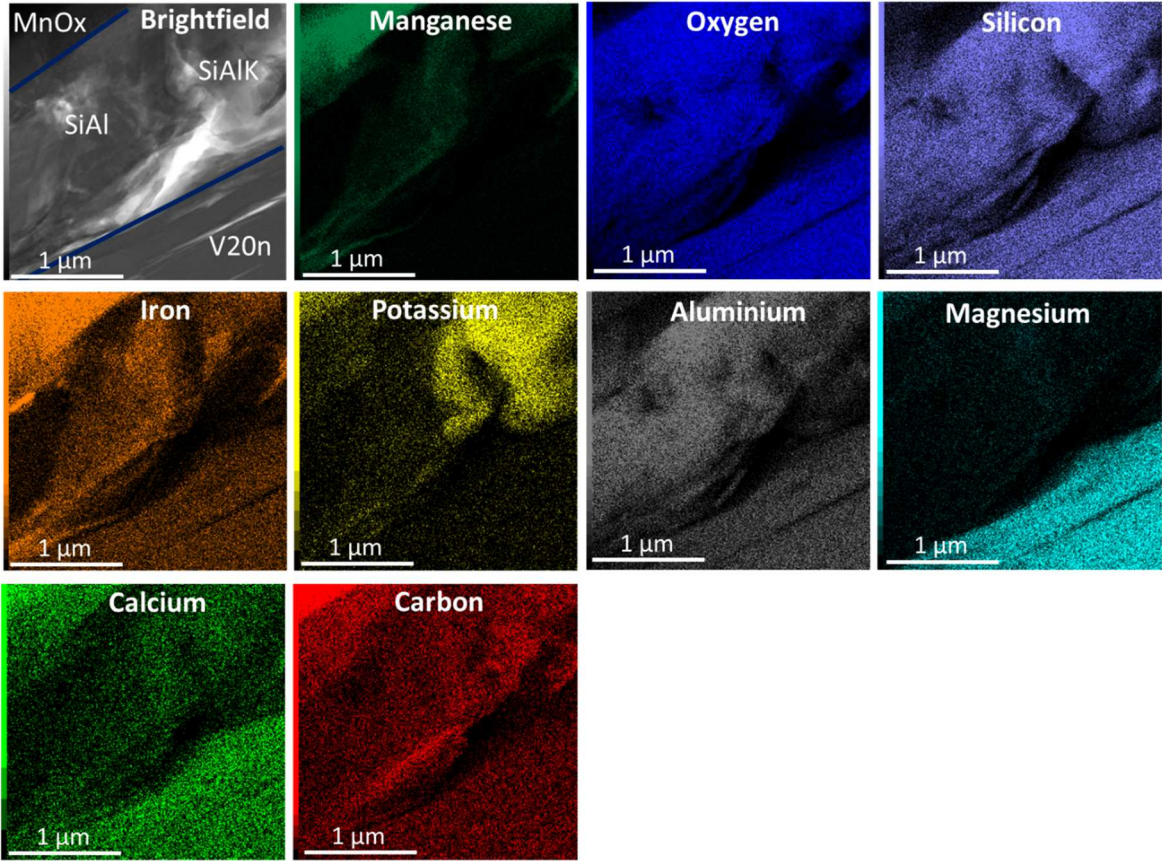1323   **Figure 5**

1324

1325   **Figure 6**

1326

1327

53
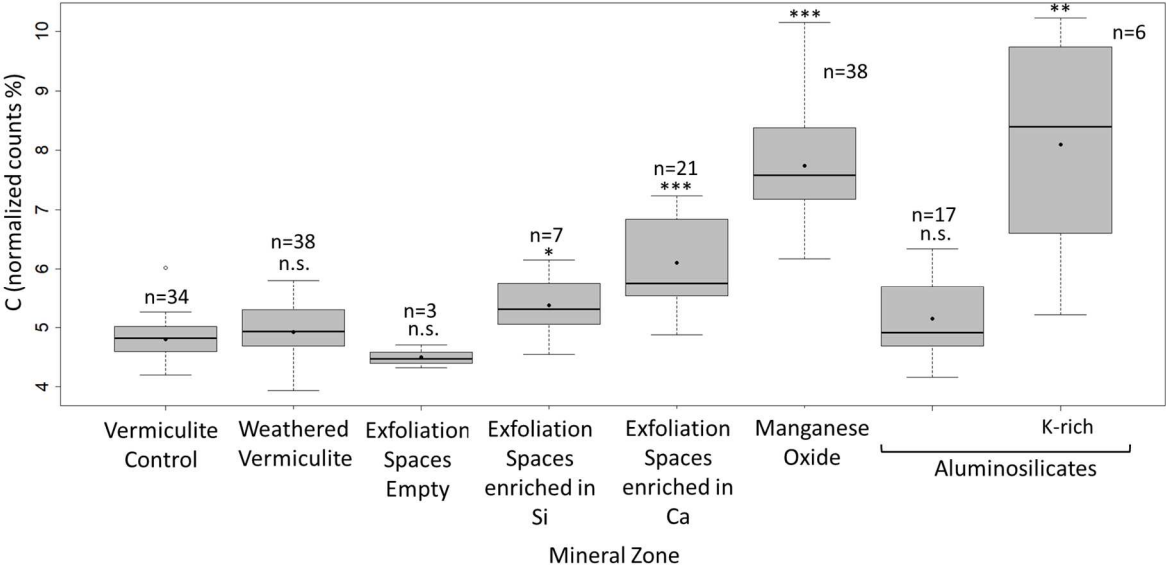
1328 **Figure 7**

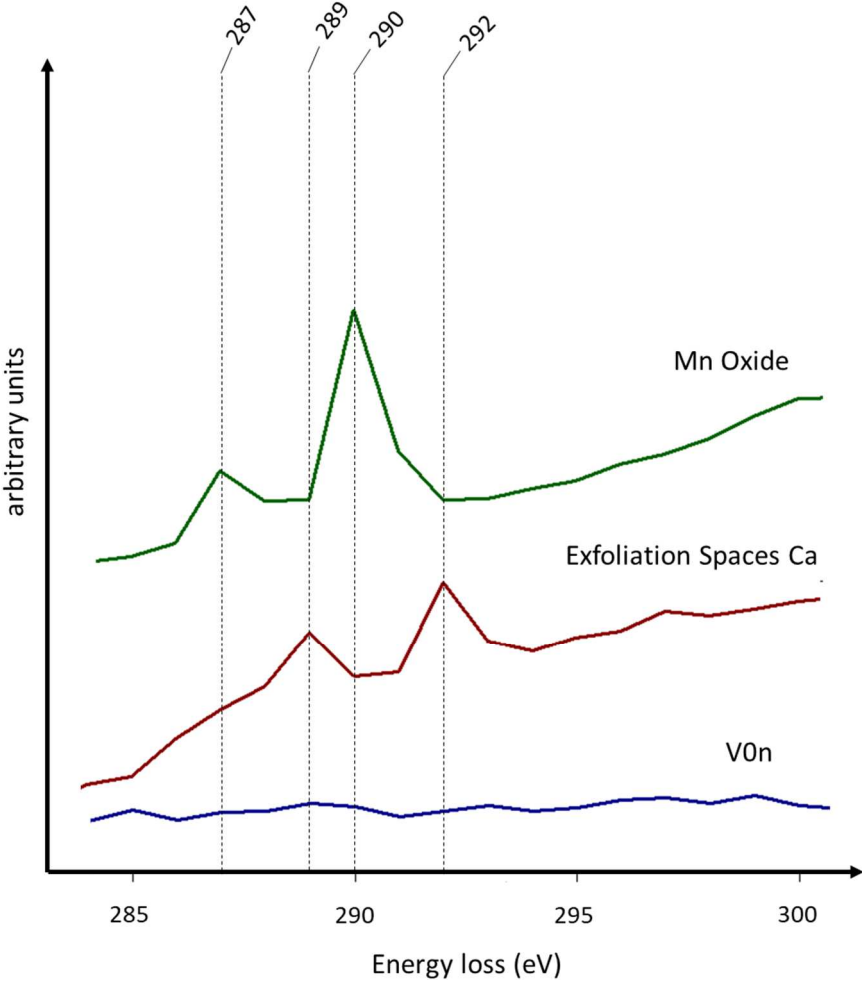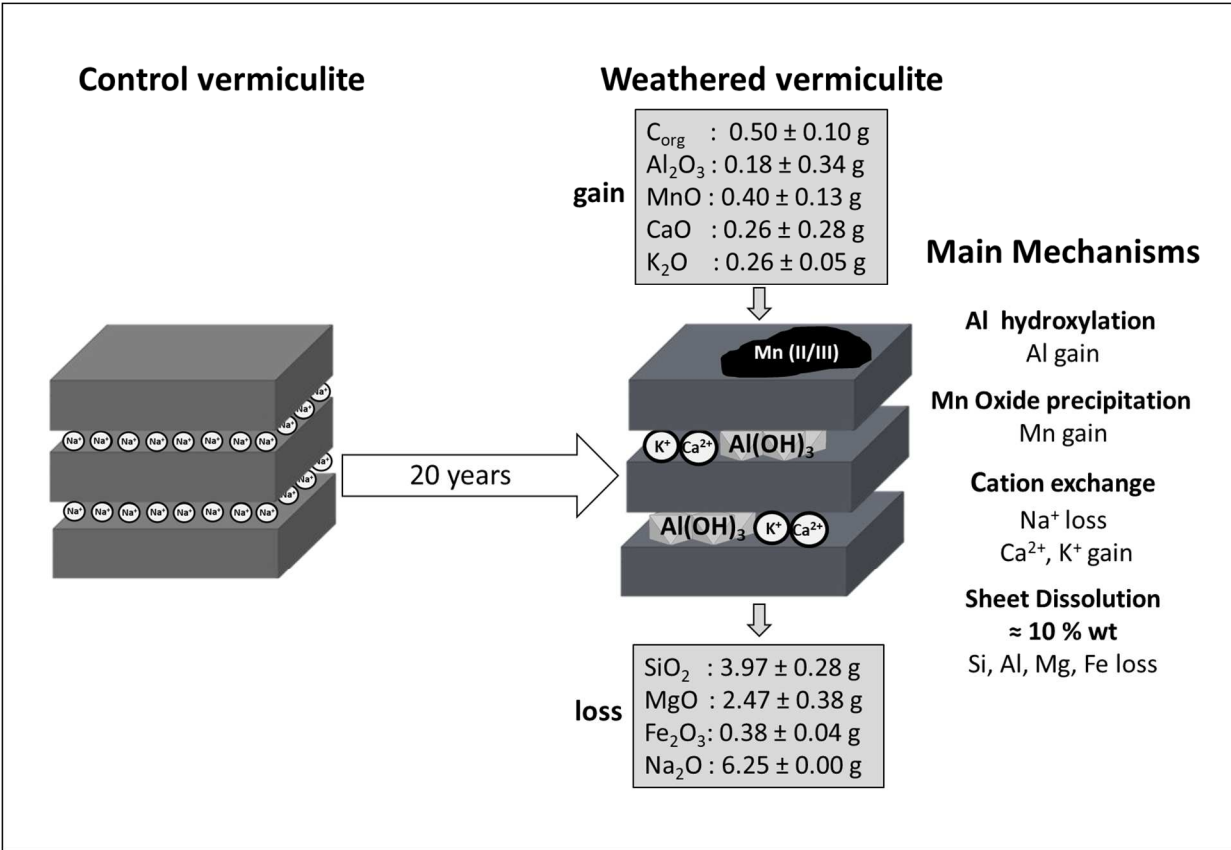
1329

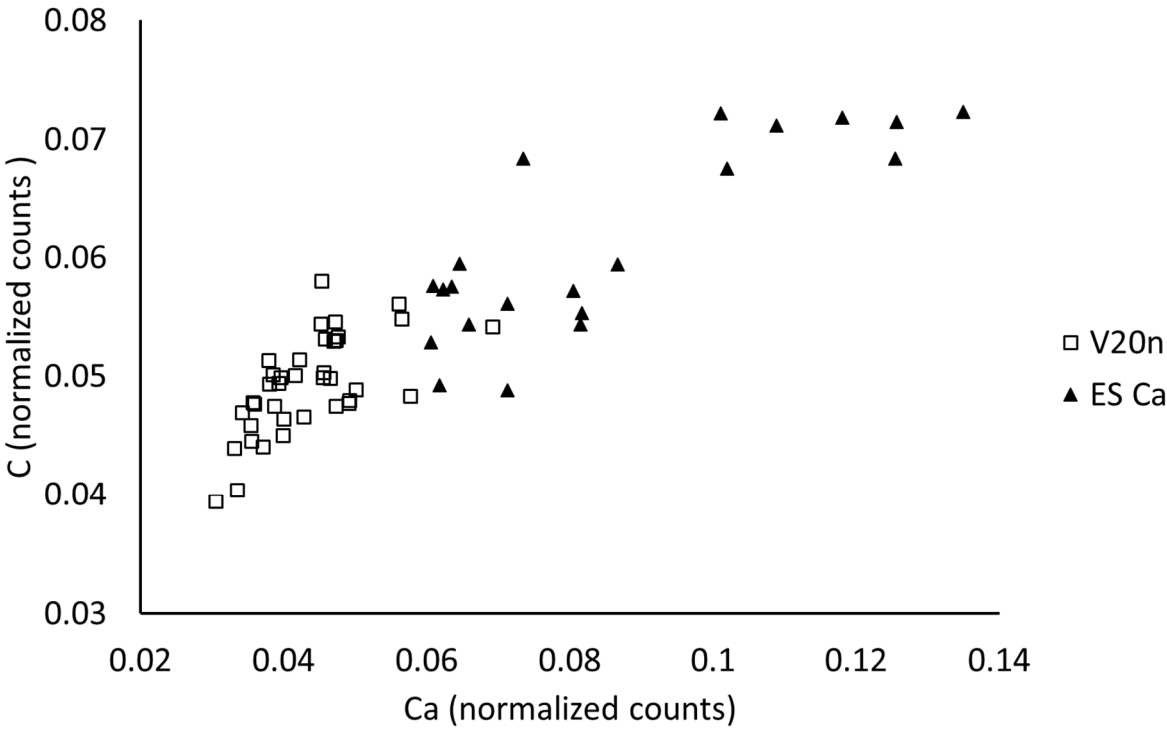1330 **Figure 8**

1331

1332

1333 **Figure 9**

1334

1335

1336   **Figure 10**

1337

1338   **Figure 11**

1339